Structural Characterization of the Taltal Segment in Northern Chile Between 22°S and 26°S Using Local Earthquake Tomography

Sergio Leon-Rios[1], Valentina Reyes-Wagner[1], Daniela Calle-Gardella[1], Andreas Rietbrock[2], Steven Roecker[3], Andrei Maksymowicz[4] and Diana Comte[1,4]

[1] Advanced Mining Technology Center, Facultad de Ciencias Físicas y Matemáticas, Universidad de Chile, Chile.

[2] Geophysical Institute, Karlsruhe Institute of Technology, Germany.

[3] Earth and Environmental Sciences, Rensselaer Polytechnic Institute, USA.

[4] Departamento de Geofísica, Facultad de Ciencias Físicas y Matemáticas, Universidad de Chile, Chile.

Keypoints

- Seismic catalog reveals forearc activity and slab dip variations. Vp anomalies in the oceanic plate are related to mid-depth seismic events.

- Velocity models uncover anomalies in Salar de Atacama and Taltal ridge that might influence seismicity distribution and hydration changes.

- Shallow low Vp/Vs (<1.75) correlate with ore deposits; deep high Vp/Vs (>1.80) suggest fluids and melting for the Lastarria volcanic complex.

Abstract

Recordings of earthquakes by a temporary deployment of 84 short period seismometers in northern Chile were used to derive regional 3D seismic velocity models for the Taltal segment. We used the Regressive ESTimator (REST) package for event detection and automatic onset estimation of P- and S-wave arrival times to create an earthquake catalog with 23,985 hypocenters. We followed standard acceptability criteria (i.e. azimuthal gap and residual cutoff) to create a high-quality dataset and inverted for 3D Vp, Vs and Vp/Vs models using local earthquake tomography.

Plots of hypocenters from the catalog, comprising 16,349 earthquakes, reveal active structures in the upper crust, dip changes along the slab and fracturing within the oceanic crust. Moreover, the wavespeed models illuminate anomalies in both the Nazca and South American plate that correlate with the observed seismicity distribution, including variations from low (1.75) to high (>1.80) Vp/Vs nearby the Atacama fault system on the coastline and the Domeyko Fault System in the forearc. The seismic velocity models also provide evidence for fluid circulation caused by the subducting Taltal ridge on the coast and partial melting feeding a volcanic complex close to the Andes. Finally, the observed low Vp/Vs ratios (~1.75) are associated with copper mining operations in the area, suggesting that this kind of imaging can be used to characterize the distribution of potential ore deposits in the area.

Plain language summary

We recorded earthquakes in northern Chile with a network of 84 seismometers and used the arrival times of P and S waves to generate 3D wavespeed models of the region. These models reveal several structures in the area, including changes in the angle of the subducting Nazca plate and fractures in the oceanic crust. Among features observed in both the Nazca and South American plates are the Atacama and Domeyko fault systems. We also infer fluid circulation caused by the subducting Taltal ridge and partial melting that is feeding a volcanic complex near the Andes. Low values of the Vp/Vs ratio are

associated with copper mining operations in the area and could be used to identify new ore deposits.

Keywords: Northern Chile, 3D Velocity Models, Tectonic Processes, Local Earthquake Tomography, Seismic Catalog, Continental Forearc

1. Introduction

The geologically active margin in northern Chile, where the oceanic Nazca plate subducts beneath the continental South American plate at a relative rate of ~66-67 mm/yr (Altamimi et al., 2016; Metois et al., 2016; Klein et al., 2018; Jarrin et al., 2022) offers an ideal setting for seismic investigations of the subduction process in tectonically erosive margins. The lack of anthropogenic noise and the dryness of the soil allow for high Signal to Noise Ratio (NSR) recordings of seismic signals. A variety of heterogeneities, such as seamounts and ridges on the oceanic crust, along with the prominent Mejillones peninsula(MP) along the coast, contribute to diverse modes by which stress in the region is accumulated and released. In particular, a number of studies have focused on the large thrust events in the area, such as the M8.0 Antofagasta earthquake in 1995 (Monfret et al., 1995; Ruegg et al., 1996; Delouis et al., 1997), the M7.8 Tocopilla earthquake in 2007 (Delouis et al., 2009; Peyrat et al., 2010; Bejar-Pizarro et al., 2010), and a proposed Mw~9.5 earthquake (Salazar et al., 2022) 3800 years ago in the Taltal segment between 22°S and 26°S (Figure 1). In the same area, long-term geodetic studies have quantified the degree of seismic coupling (Chlieh et al., 2004; Metois et al., 2013; Metois et al., 2016; Klein et al., 2018) and the capacity of the area to host a large megathrust earthquake (Yañez-Cuadra et al., 2022). Several recent investigations have focused on understanding the type and mechanisms of the seismicity in northern Chile. For example, Mavor et al. (2020) described the kinematics and tectonic evolution of the Taltal Fault, Sippl et al. (2023) used a 15-year seismic catalog to summarize the activity in northern Chile, and Gonzalez-Vidal et al. (2023) deployed a temporary network to explore the relations between heterogeneity in the subducting plate and the degree of interplate locking. In terms of seismic imaging of this zone, Husen et al. (2000), together with Haberland and Rietbrock (2001), set foundations for tomographic analysis by deriving seismic velocity and attenuation models, respectively. However, despite these efforts, there are still gaps where tectonic processes on a regional scale - from the coastline to the volcanic arc - have not been addressed.

To investigate the roles that features such as a subducting ridge and crustal faults play in the overall tectonics and in the high intermediate-depth seismicity rate of the Taltal segment, we analyzed data from a passive seismic experiment comprising a large network of seismic sensors. The size and the density of this temporary deployment along with the high rate of seismicity in this area (e.g., Centro Sismólogico Nacional (CSN) technical report for the seismicity in Chile 2018, 2019, 2020; www.csn.uchile.cl) facilitates applications of high-resolution imaging using local earthquake tomography (LET). This method uses the arrival times of P- and S-phases generated by local earthquakes to derive 3D seismic velocity models for Vp, Vs and Vp/Vs that highlight the structures and anomalies in the subsurface (e.g., Aki and Lee, 1976; Eberhart-Phillips et al., 1986; Thurber et al., 1995). In this study, we apply this type of analysis to investigate the distribution of fluids in the Taltal segment and its potential relation to the seismic activity between and within the oceanic and the continental plates. The large amount of seismic data recorded by this deployment allows us to fill the gap left by recent studies by Sippl et al. (2023) and Gonzalez-Vidal et al. (2023). Furthermore, the high-quality dataset led us to better resolve and image the main geological structures towards the arc and areas of fluid circulation that control the seismic activity at shallow- (<30 km) and intermediate-depth (~100-200 km) in the segment.

2. Tectonic setting

During the past century, large to great earthquakes (7.5-8.5) have been documented in the Taltal segment (Figure 1). These include the intraplate M8.0 Calama earthquake in 1950 (Kausel & Campos, 1992), the M7.7 and M7.6 Taltal earthquakes in 1966

(Deschamps, 1980) and 1987 (Ruiz and Madariaga, 2018), the interplate M8.1 Antofagasta earthquake in 1995 (Monfret et al., 1995; Ruegg et al., 1996; Delouis et al., 1997) and the interplate M7.7 Tocopilla earthquake in 2007 (Delouis et al., 2009; Bejar-Pizarro et al., 2010; Peyrat et al., 2010); all of them located in the northern part of the segment (22°S-25°S). Only two documented megathrust earthquakes struck the southern part of this region in 1918 (M~7.5-7.7, Ruiz and Madariaga, 2018; Metois et al., 2012) and 1922 (M~8.5, Willis 1929; Abe 1979; Beck, 1998; Comte et al., 2002; Kanamori et al., 2019), which, due the absence of megathrust events with M>8.5 in the past (Ruiz and Madariaga, 2018) has led to some authors to refer to this portion of the segment (25°S-27°S) as atypical for the Chilean margin. At the same time, the multidisciplinary study of Salazar et al. (2022) inferred that, based on the effects on ancient inhabitants, a large earthquake and tsunami occurred ~3800 yrs ago, suggesting that the area is capable of hosting large megathrust earthquakes similar to the 2010 Maule and 1960 Valdivia event in other regions of Chile (e.g., Kelleher, 1972; Ruiz & Madariaga, 2018). While megathrusts earthquakes are infrequent, swarms of seismicity are common in this area (Comte et al., 2002; Holtkamp et al., 2011; Metois et al., 2016) suggesting that heterogeneities along the plate interface complicate this portion of the Taltal segment.

Offshore, irregularities in the bathymetry of the seafloor such as the Mejillones Fracture Zone (MFZ, Maksymowicz 2015) and the Taltal ridge (Figure 1a) have been proposed to cause a seismogenic segmentation in the region that stops the rupture propagation of local megathrust earthquakes (Maksymowicz, 2015). Pasten-Araya et al. (2021) discussed the presence of a splay fault close to the coastline in the region and emphasized the importance of these types of structures for seismic hazards. Onshore (Figure 1a), the region has two main N-S fault systems, the Atacama fault system (AFS) and Domeyko fault system (DFS), that were formed in response to an oblique transfer of subduction stress (Mavor et al., 2020 and reference therein). The upper-crust is further complicated by several other geological structures with diverse lineaments and lengths, such as the Mejillones fault (MF), the Taltal fault (TTF), the Calama-Olacapato-El Toro lineament (COT) and others (Figure 1a; Arabasz 1968; Arabasz Jr, 1971). These features have not been well imaged and should play a critical role in the behavior of crustal seismicity and in the distribution of abundant porphyry copper deposits (Cooke et al., 2005; Richards, 2016).

The volcanic arc in the central part of the segment (~23.0°S – 24.5°S) is shifted towards the east relative to its position to the north and south (Figure 1a), which has been explained by a region of high-density located below the Salar de Atacama (Götze and Krause, 2002; Schurr and Rietbrock, 2004). Finally, to the east, an analysis of electrical resistivity (Diaz et al., 2012; Pritchard et al., 2018; Kühn et al., 2018; Araya-Vargas et al., 2019) and receiver function studies (Ward et al., 2017; Delph et al., 2017) show two large magmatic bodies, Altiplano-Puna (APMB) and Lazufre (LMB), located at the margins of the area of interest.

3. Data and Methods

Dataset: The Taltal seismic experiment

The data analyzed in this study were recorded by a temporary network deployed as part of a joint effort between the Advanced Mining Technology Center (AMTC) of Universidad de Chile and the Geophysical Institute from the Karlsruhe Institute of Technology (KIT) of Germany and comprised 84 triaxial short period geophones (3D Geophone HL-6B, 4.5 Hz) and Datacube[3] digitizers sampling at 200 Hz. The instruments covered an area of ~127,000 km^2 and operated between March and October 2020 (Figure 1b).

Seismic catalog and onset detection

The seismic traces recorded by the Taltal experiment were processed using the Regressive ESTimator (REST) automatic picking package described in Comte et al. (2019), Reyes-Wagner et al. (2023) and summarized in Supporting Information 1. REST uses the autoregressive approach of Pisarenko et al. (1987) and Kushnir et al. (1990), combined with data windowing procedures suggested by Rawles and Thurber (2015). By having a reference wavespeed model for the area to investigate, REST can predict arrival times, to an accuracy of a few (~ 5) seconds, from either probable hypocenters or known sources to mitigate false positives. The estimation function is sensitive to changes in both amplitude and frequency and hence benefits from sources that emit a broad spectrum of energy that can be used to discriminate signal from noise. For the same reason, it generally works better when the seismograms are not filtered. Hypocenters are determined using a grid search location scheme (Roecker et al., 2004; 2006; see Supporting Information 1) over a 3D distribution of nodes in a spherical coordinate system.

In this study, we adopted a reference 1D velocity model based on the results of Husen et al. (1999) for depths down to 50 km and IASP91 (Kennett & Engdahl, 1991) for depths > 50 km. Wavespeeds and travel times are specified on a 3D grid of 157,500 nodes separated by 10 km over an area of 700 x 750 km^2 and 285 km depth. Events included in the inversion were required to have a minimum of 10 phases and an arrival time residual between -2.0 s and 2.0 s, resulting in an initial catalog of 23,985 earthquakes with 774,989 P- and 667,114 S-wave arrival times with an overall root mean square (RMS) residual of 0.48 s. In carrying out the LET, we further refine the catalog by applying a stricter selection criterion requiring (1) an azimuthal gap in recording stations of less than 210°, (2) a minimum of 20 total phases, and (3) a maximum residual of 1.5 s. The refined catalog contains 12,692 earthquakes with 415,425 P and 358,770 S arrival times.

Three-dimensional seismic velocity models

The arrival times in the refined catalog were used to generate a 3D velocity model for Vp and Vp/Vs using the joint inversion methodology described in Roecker et al. (2004, 2006; see Supporting Information 2). The algorithm parametrizes the subsurface as a volumetric grid in a spherical coordinate system and performs an iterative process that jointly inverts for earthquake locations, Vp, and either Vs or Vp/Vs. The process stops after the reduction in the residual variance becomes statistically insignificant.

The grid has 677,376 nodes spaced at 5 km and covers an area of 540 x 560 km^2 from the surface to a depth of 270 km. The initial Vp model is the same 1D model used to generate the catalog, and an initial Vp/Vs of 1.77 estimated from a Wadati diagram (Wadati et al., 1933; Kisslinger and Engdahl, 1973; Supporting Information 3) of P and S arrival times. An optimal damping factor is estimated using trade-off curves (Supporting Information 4) of residual and model variance, the latter being defined using the “roughness” parameter of Greenfield et al. (2016). The preferred model is obtained after 16 iterations showing an overall RMS of 0.25 and a variance of 0.15. (Supporting Information 5). These values represent a decrease of about 37% in RMS and 45% in variance compared to those from the initial model. Final hypocenters – used in the inversion process – have average arrival time residuals of 0.13 s and 0.49 s for P-and S-wave onsets (Supporting Information 6), respectively. Location uncertainties estimated from marginal probability density functions are on the order of 6 km, 5 km, and 8 km for the east, north and depth coordinates, respectively. For the complete catalog – comprising 16,349 events with the inclusion of the events at depths > 180-200 km – the location errors increase to 7 km longitude, 6 km in latitude and 10 km in depth. The latter is the catalog on which this study bases the discussion.

Model Resolution

The irregular distribution of both stations and earthquakes and the highly nonlinear nature of the inverse problem requires that we document how resolution varies within the model volume. Most common ways to assess the resolution of seismic velocity models are the checkerboard test (e.g., Spakman and Nolet, 1988), bootstrap resampling (e.g., Calvert et al.,2000; Hicks et al., 2014; León-Ríos et al., 2021) and reconstruction test (Rawlinson and Spakman, 2016). For all cases, synthetic data are calculated in hypothetical models with different sizes of velocity anomalies. Small anomaly size (~5 km) can be tested to explore the lower limit of resolution, while medium and large sizes (15 km and 30 km) are helpful to assess the resolution based on the average station spacing. Moreover, by testing different sizes, we can also detect the lack of resolution and smearing across a range of plausible scales (Inoue et al.,1990; Fukao et a., 1992; Rawlinson et al., 2016). Random noise based on the standard deviation is typically added to the synthetic data to simulate actual data quality (e.g., Hicks et al., 2014; Comte et al., 2019). These synthetic datasets are then inverted following the same procedure as that for the real data and a comparison between the actual and recovered models is made to evaluate resolution scale lengths.

Checkerboard test

The checkerboard resolution tests assumed equi-dimensional anomalies of 15 km, 20 km and 30 km length scale, within which velocities were perturbed by ±5% to form a checkerboard pattern (Supporting Information 7, 8, 9 and 10). Gaussian noise of 1/3 σ of arrival time residuals was added to the synthetic data at a level commensurate with the anticipated uncertainties in the observations, and the result was inverted following the same procedure as that for the actual model. The results for the 15 km dimension anomaly show that it is possible to recover the initial perturbations in much of the model volume at this scale. In general, we infer that the data is capable of recovering wavespeed variations at this scale down to 150 km with a geometry consistent with the shape of the subduction margin. Tests performed with smaller dimension perturbations indicate that 15 km anomalies are the smallest size for interpreting possible geological structures.

Bootstrap resampling

The bootstrapping technique is useful to assess the sensitivity of seismic velocity models with respect to the completeness of the event catalog. The bootstrap resampling method suggests that event-based resampling should produce similar results to resampling individual picks (e.g., Calvert et al., 2000; Hicks et al., 2014). We randomly selected 80% of the events in the original data and inverted following the same procedure as for the actual models. Resulting Vp, Vs and Vp/Vs seismic velocity models (see Supporting Information 11) recover most of the anomalies observed in the actual models indicating that the results are insensitive to the event selection criteria. Uncertainties estimated from the bootstrapped resampling are about ±0.025 km/s for Vp and Vs and about ±0.004 for Vp/Vs.

Reconstruction Test

While the idea to recover and/or resemble some known geological features such as subducting slabs or isolated perturbation observed in the preferred model is reasonable, the reconstruction of prismatic pattern includes effects that can only be valid if the internal structure of the study area has in effect an alternated prismatic disposition (Comte et al., 2016; Rawlinson and Spakman, 2016). An alternative way to assess the capacity of a dataset to recover interpretable features at the scale and amplitude as those that appear in the model is to reconstruct the same distribution of imaged anomalies (e.g. Prevot et al. 1991). To do so, we generated a synthetic dataset using the same source–receiver distribution as the actual dataset and followed the same iterative procedure as with real data to attempt to recover the preferred model from a 1-D starting model.

The results show that the synthetic dataset is able to recover most of the anomalies both in velocity and amplitude (see Supporting Information 12). The northern profiles (P1-P3) show that offshore resolution can suffer from lateral smearing and therefore reduced resolution. This can be explained by the lack of stations in the area which prevents the model from accurately resolving the absolute velocities. At greater depths (~100 km) the synthetic data is able to recover with almost exactly the same amplitude the anomalies observed by the actual model. Similarly, the central (P4-P5) and southern profiles (P6-P8) recover most of the anomalies, with few exceptions offshore (P8) related to the lack of observations in the area.

4. Results

Hypocenter catalog

The catalog of well constrained locations has 16,349 events with an average location uncertainty of 6.90 km (7 km longitude, 6 km in latitude and 10 km in depth). Most of the events with depths between 30 km to 120 km depth are located along the subduction interface (slab 2.0, Hayes et al., 2018; Figure 2 and 3). Earthquakes in the northern part of the model (cross sections P1-P4) are predominantly intermediate-depth (80 km – 120 km depth), while those in the south (cross-sections P5-P8) are more evenly distributed along the plate interface. The northernmost sections (P1 and P2) include upper crustal shallow (<10 km) activity mostly from mining operations (Figure 2). However, there is seismicity that correlates spatially with both the Atacama and Domeyko fault systems, and that it is consistent with the active nature of these large-scale systems (Bloch et al., 2014; Sippl et al., 2018; Figure 4). Although the in-depth distribution cannot be interpreted as the actual geometry of the faults, the observation of seismicity in these large structures offers an important opportunity to perform small-scale experiments to better characterize these features. Section P2 also shows a cluster of seismicity at the coast located within the Nazca plate at ~40 km depth that is consistent with the Michilla cluster identified in previous catalogues from Fuenzalida et al. (2013) and Pasten-Araya et al. (2021) after the 2007 Tocopilla earthquake. At greater depths (~80 – 110 km), clusters of seismicity (C1 in Figure 3) are found within the Nazca plate. This activity, with ~2800 events registered, shows a rms of 0.456 s and vertical errors of ~7 km. An additional dense cluster of seismicity evident in section P4 (Figure 3) corresponds to the Jujuy seismic nest (Valenzuela-Malebran et al. 2022). Compared with the Slab2 model (Hayes et al., 2018), our seismic catalog suggests a change in dip of the subducting Nazca plate at depths between 100 km - 150 km in the northern profiles (P1-P4). Similar variations in the dip angle have been previously reported by Sippl et al. (2019). We observe seismicity at shallower depths (<50 km) in section P4-P5 at a distance of ~400 km from the trench that might be related to volcanic activity from either the Lazufre magmatic body or the Altiplano-Puna magmatic body (Ward et al., 2014; 2017). The seismicity is distributed between 5 km and 70 km depth and has location estimation errors of ~19 km in depth, mostly explained by the coarse station distribution in the eastern part of our area of study. In sections southward from the Mejillones Peninsula (P6 to P8, Figure 2) the seismicity appears to be distributed in lineaments striking north-northwest, in concordance with structures observed both onshore in the upper plate (Figure 1; Mavor et al. 2020, and references therein) and offshore (Supporting Information 13; Gonzalez-Vidal et al., 2023), while to the north the seismicity presents a more heterogenous distribution. Similar NNW seismicity lineaments have been observed to the north (~24°S) by Pasten-Araya et al. (2021), who related the seismic activity to splay faults. These observations suggest a regional structural pattern in this segment of the margin and could reflect a latitudinal segmentation of the active structures near the interplate boundary, which when considering the coverage of our relocated catalog might be associated to: (1) the northern limit of the Taltal ridge, (2) the migration of the Taltal ridge as described by Bello-Gonzalez et al. (2018), and (3) the obliquity of the AFS in the area (Mavor et al. (2020)). Whatever the actual causes for the seismic distribution are, further studies are necessary to better constrain the earthquake locations and its causes.

Seismic tomography

First order structures observed in the tomographic models (Figure 5 and 6 for absolute Vp and Vp/Vs values, Supporting Information 14 and 15 for Vs and percentage values, respectively) include the Nazca plate imaged to depths of ~150 km with an east dipping anomaly of elevated wavespeeds. The South American plate shows Vp values of ~5.0-7.0 km/s and Vs ~3.0 - 4.0 km/s which are consistent with those found in previous investigations (Husen et al., 2000; Haberland and Rietbrock, 2001; Schurr et al., 2006; Pasten-Araya et al., 2021). The average value of Vp/Vs determined with the Wadati diagram (Wadati et al., 1933; Vp/Vs=1.77) is retained in the inversion. The continental Moho discontinuity associated with Vp ~7.5km/s implies a crustal thickness of the South American plate of around 40 – 50 km below the forearc, which is consistent with previous observations (e.g., Husen et al., 2000; Haberland et al., 2001; Tassara and Echaurren, 2012). We observe a heterogeneous distribution of anomalies in the whole segment with several transition areas from high (Vp/Vs >1.77) to low (Vp/Vs <1.77) ratios observed in both lower and upper plate (Figure 5 and 6). These anomalies and transition areas can be correlated with geological structures observed at the surface, such as the AFS, DFS, the Salar de Atacama, and the Salar Punta Negra (see section z=10 km in Figure 6).

In a closer view of the continental crust, section P1 (Figure 4) shows a heterogeneous velocity structure with Vp ~6.0 km/s in the first 10 km depth and between 6.0 -7.0 km/s at 10 – 30 km depth. The Vp/Vs model shows an anomaly (>1.80; labeled A1 in Figure 5 and 6) located at the coastline in the upper crust. Eastward, the model shows a low Vp/Vs patch (<1.74; labeled A2 in Figure 5 and 6), that extends along the whole segment at ~69°W from near the surface to 30 km depth. In section P2 the upper crust shows a more heterogeneous forearc between 200 – 300 km from the trench with Vp~6.5 km/s down to 30 km depth and alternating patches with low and high Vp/Vs regions. In particular, the Vp/Vs model illuminates two anomalies with high (>1.82) and low (<1.75) ratios located at shallow depths which are coincident with the location of the Salar de Atacama (Figure 7 – salar de Atacama). Continuing to the south, sections P3 to P6 for Vp/Vs show two large patches (A2, A5) with low ratios (<1.75) which are contoured by sub-vertical elongated anomalies (Vp/Vs>1.77) that reach down to the plate interface. Another unusual vertical-elongated feature appears at 24°-24.5°S, in section P4 and P5, below the Cordillera de los Andes. This anomaly (A6, Figure 8 - volcanic), with Vp/Vs~1.80, is accompanied by shallow seismicity and is coincident with a low resistivity feature identified by other geophysical studies in the area (Diaz et al., 2012; Araya-Vargas et al., 2019).

In the region of the Andean wedge, at ~300 km eastward from the trench, interplate boundary and subducted plate, P1 shows an area of Vp~8.0 km/s close to the plate interface at 50 km depth that locates above a cluster of seismicity within the Nazca plate (Figure 5). At greater depths (>80 – 100 km), we observe a large (150 km width x 40 km depth) low Vp/Vs (<1.80; Figure 9 – deep cluster) which correlates with the clustered seismicity within the oceanic crust. We note that previous studies have identified Vp/Vs ratios with similar values (Herrera et al., 2023). These reduced Vp/Vs values suggest a more rigid and dehydrated slab prone to break and to generate localized increase in intermediate-depth seismic activity. In section P2, the 8.0 km/s Vp east-dipping-contour shifts upwards in comparison to P1. In this section, at distances >300 km from the trench and at ~50-70 km depth, we find areas with Vp values ~ 7.5-7.7 km/s that illuminate the mantle wedge that are consistent with values suggested by Comte et al. (2023). In sections P3 to P6, Vp in the lower part of the oceanic plate has a value of 8.2 km/s (labeled A4 in Figure 5). The oceanic slab here has Vp/Vs ratios > 1.82, distinguishing it from the slab in the northern profiles. Sections P6, P7 and P8 show a westward shift of the Andean wedge marked by the Vp~7.6-7.8 km/s contours at a distance about 300 km from the trench. Vp/Vs in the vicinity of the Taltal ridge in sections P6 and P7 (labeled A7 in Figure 5) is low (<1.76). Finally, sections P7 and P8 show a large high (>1.80) Vp/Vs anomaly (labeled A8 in Figure 5 and 6) that extends for about 100 km in the upper crust.

5. Interpretation and Discussion

Large-scale upper-crust features

The continental crust shows a sequence of low and high Vp/Vs anomalies (Figure 5). Along the coastal area, and correlating with the AFS, most of the profiles show high Vp/Vs values that could be associated with a more fractured crust due to this fault system. This correlation is particularly evident northward of ~25°S (Figure 4 and 5). In contrast, the coastal area in the zone of the Taltal ridge subduction (P6-P8 in Figure 4) is characterized by low Vp/Vs values which could be explained as a change in fluid transport inside the crust above this subducted feature. Coincidently, the seismic anomalies in Vp/Vs associated with the AFS show local rotations (Figure 6) in this zone which also matches with the geography of the coastline and the trend of the AFS in the area. In a similar way, at distances of ~200 km – 250 km from the trench (Figure 5), we observe another high Vp/Vs zone that coincides with the DFS. Based on our evidence, we suggest that this large-scale feature is generating seismicity down to ~30 km depth (Figure 4), which needs to be studied more carefully. Additionally, the Vp/Vs model suggests that the roots of the DFS may extend to a depth of ~50 km. The latter is consistent with the distribution of large porphyry copper deposits in the region (Reutter et al., 1991, 1996; Tomlinson and Blanco, 1997a; 1997b; Camus and Dilles, 2001). Eastward from the DFS, low Vp/Vs anomalies (A1-A4, <1.80; Figure 5 and 6) may be associated with an ancient magmatic arc that might have metamorphosed the surrounding area (e.g. Diaz et al., 2012) and contributed to the accumulation of porphyry copper deposits (Comte et al., 2023; Chen and Wu, 2020). This observation coincides with the location of large copper mining operations in the area such as Chuquicamata, Gabriela Mistral and Escondida, and suggests that LET technique can be used as a tool to complement the exploration and characterization of porphyry copper deposits at greater depths (Comte et al., 2023). In terms of absolute Vp velocity, and at crustal depths (< 50 km), the DFS is in general correlated with a transition from high Vp to the west to low Vp to the east of this structural limit, which could reflect a west-east thermal gradient related to active magmatic arc and subduction geometry (Contreras-Reyes et al., 2021) and/or the presence of high density basement units related to ancient volcanic arcs westward from the DFS (Bascuñán et al., 2016).

The presence of cold and dense basement westward from the DFS is concordant with the more rigid (low Vp/Vs) crust observed between the AFS and DFS (Figures 5 and 6). East of the DFS, Vp/Vs values show a more heterogeneous distribution with low Vp/Vs anomalies in the southern portion of the Salar de Atacama basin (SdA) and to the southeast of the Salar de Punta Negra basin (Figure 5). These low Vp/Vs anomalies could be interpreted as more rigid, cold or less fractured zone of the crust. By contrast, higher Vp/Vs anomalies are located to the north of the SdA (Figure 7). This heterogeneous distribution in Vp/Vs could be related to the variability of lithology, age, and fracturing of the ancient basements in this region (e.g. Niemeyer et al., 2018) and to the presence of regional structures, as the northwest Calama-Olacapato-El Toro lineament (COT, Lindsay et al., 2001) that could control changes in fracturing and fluid contents of the crust between the northern and southern portions of the SdA region (Figure 7). Under this interpretation, the rigid zones with relatively low Vp/Vs (and high Vp values) seem to be rounded by large structures associated with high Vp/Vs and low Vp values. In general, our model shows that mantle and crust do not present a clear and uniform high Vp velocity anomaly below the Salar de Atacama basin, which suggest that this region is not particularly strong, at least in the sense of high Vp values (and related high-density values).

At a regional scale, the succession of bands with different Vp/Vs (roughly with north-south strike) in the forearc correlates well with large scale electric resistivity anomalies observed in magnetotellurics studies of the zone (Slezak et al., 2021; Contreras-Reyes et al., 2021), where crustal high Vp/Vs, interpreted as fractured and/or hydrated zones of the crust, correlate with low resistivity zones associated with large-scale crustal structures (the AFS and the DFS).

Subducted slab, Mantle wedge and Fluid circulation

First-order observations suggest an along strike variation in the content of fluids (related to elevated Vp/Vs) along the oceanic slab. While profiles P1-P2, at around 200 km from the trench, show small areas of elevated Vp/Vs (> 1.77), the central and south profiles show anomalies with Vp/Vs~1.80 around the same distance suggesting a more hydrated slab to the southern part of the Taltal segment (Figure 5). One of the causes for this segmentation might be associated with the Mejillones peninsula and/or the MFZ as previously suggested by Maksymowicz (2015, Supporting Information 16 and 17), however further studies need to be conducted to provide an answer on this matter and to assess the role of these large structures. At greater depths (>100 km), we also observe changes with strike. P1-P3 show anomalies of low Vp/Vs (<1.76), P4 and P5 show elevated ratios, and P6-P7 show back again reduced Vp/Vs although with smaller amplitude in comparison to the northern ones. In specific, P1 is accompanied by clustered seismicity (Figure 9) aligned with a sub-vertical orientation. We note that previous studies have identified Vp/Vs ratios with similar values (Herrera et al., 2023). Furthermore, the transition from hydrated (high Vp/Vs) to dehydrated (lower Vp/Vs <1.76) is consistent with temperature and pressure at these depths (Haberland and Rietbrock, 2001). The observed low Vp/Vs block and the dip change in the deeper part of the slab (Figure 9) might suggest a more brittle behavior of the slab at these depths favoring the fracture of the plate by creating fissures or cracks and subsequently causing a localized increase in intermediate-depth seismic activity (Figure 10).

Another fluid related seismic anomaly can be observed in profiles P7-P8 with a high Vp/Vs anomaly (labeled A8 in Figure 5 and 6). Here, we clearly observe a transition from a low (1.76-1.72) Vp/Vs anomaly (A7) located offshore to higher values of Vp/Vs (>1.80) onshore. The latter is more prominent at greater depths (~50 km) . We attribute this variation of seismic anomalies to an increase in the fluid circulation promoted by the Taltal ridge, which subducts between ~25°S – 26°S. The subduction of this type of topography enhances the fracturing of the slab, promoting seismicity in the surroundings (Collot et al., 2004). A similar behavior has been described for subducted seamounts in Ecuador (Carnegie ridge; Leon-Rios et al., 2021) and Costa Rica (Husen et al., 2002). Furthermore, the presence of large-scale, shallow oceanic features can cause basal erosion and fractures in the overriding plate (Scholz and Small, 1997; Contreras-Reyes et al., 2011) enhancing the transport of fluids from deeper to shallower depths (Figure 10; Collot et al., 2004; Marcaillou et al., 2016; Leon-Rios et al., 2021).

Finally, profiles P4 and P5 show an elongated anomaly (labeled A6) with Vp/Vs~1.79 - 1.80 located at 50 km depth, in the continental mantle, and ~ 300 km from the trench (Figure 8). We interpret this feature as fluids moving upwards from the plate interface towards the surface, promoting partial melting and feeding the northern edge of the LMB and other volcanic complexes (Haberland and Rietbrock, 2001; Diaz et al., 2006; 2012; Araya, 2019). The shallow seismicity observed ~400 km from the trench corroborates the hypothesis of fluid circulation in the area. We note that the SdA area (around profile P3-P4, Figure 5) correlates well with a part of the continental mantle (depth ≥ 50 km) characterized by high Vp (>8.0 km/s) and low Vp/Vs (<1.70) bounded by low Vp (~7.5 km/s) and high Vp/Vs (>1.80), which suggest a correlation between anomalies associated with high fluid content (and high temperatures) and the active volcanism in the area, including the local eastward migration of the volcanic arc around the SdA (Figure 10).

Conclusion

Data from ~23,000 earthquakes recorded by a large temporary deployment that operated in northern Chile for an 8-month period allowed us to summarize the heterogeneous seismotectonics of the Taltal segment in northern Chile. We applied LET to jointly derive 3D seismic velocity models for Vp, Vs and Vp/Vs and earthquake locations; and combined the results with other geophysics methods and geology studies to explore the role that the Atacama and Domeyko fault zones, and the Taltal ridge might have in controlling the overall tectonics of the margin.

Seismicity distributes mostly along the slab interface where we observe patches of low Vp/Vs that together with a dip change might contribute to cause constant and clustered seismic activity. Offshore, we observe clustered seismicity that we relate to two possible causes: (1) splay faults that reach the slab interface and/or (2) the stress transfer caused by the subducting Taltal ridge. Also, we observe the active nature of large-scale structures in the overriding plate such as the Atacama and Domeyko fault systems. Both features appear to reach down to the seismogenic zone as shown by the change from reduced (<1.77) to elevated (>1.77) ratios in the Vp/Vs model. These large upper crust faults also seem to have a major control over the distribution of porphyry copper deposits. Furthermore, low Vp/Vs anomalies (<1.75) at shallow depths (<20 km) collocate with sites of large copper mining operations which are bounded by both the AFS and DFS. This observation suggests the use of LET to shed light on possible mining exploration targets. However, further studies are needed to better constrain the actual role that upper crust faults have in the overall tectonics, as well as their in-depth extent and geometry.

In terms of fluids, the oceanic slab shows a transition from elevated (>1.80) to reduced (<1.76) Vp/Vs suggesting a highly hydrated plate at seismogenic depths that dehydrates and evolves into a dryer and more rigid and brittle slab at greater depths. The latter, together with the observed dip change and the fluids migrating to the mantle might contribute to explaining the persistent high rate of intraplate seismicity observed at ~100 km depth. Furthermore, these changes in hydration are also observed along strike with the northern part of the segment being less hydrated than the southern portion. Again, the heterogeneous tectonic setting of the area seems to be the main control of this behavior. To the north, the Mejillones Fracture Zone and the Mejillones Peninsula might act as a barrier for fluid transportation, while to the south the Taltal ridge swell enhances the circulation of fluids by eroding and fracturing the southern edge of overriding plate along the slab. Towards the Andes and at greater depths (~100 km), the velocity models also suggest the presence of fluids (high Vp/Vs) that we relate with partial melting feeding the Lazufre Magmatic Body and other volcanic systems such as the Lascar volcano.

Acknowledgments

The authors acknowledge the funding from Fondecyt Postdoctorado 2022, No 322099; NSF-China-ANID PI18003; PIA AFB220002. Alejandro Faundez and Gerardo Peña who assisted in the network deployment. Section profiles and map view figures were made using GMTv5 (Wessel et al., 2013) and colored following the guidelines for CVD accessibility by Crameri et al. (2020).

Data availability

Temporary X5-Taltal network details in FDSN database (Rietbrock et al., 2020). Raw data will be available at the FDSN/EIDA server hosted by GFZ-Potsdam (Rietbrock, 2024) (DOI: 10.35097/dIDjKJPeUpZFWjbQ). Initial and final models as well as hypocenter catalog, arrival times and processing algorithms user guides are available in ZENODO (Leon-Rios, 2023; https://doi.org/10.5281/zenodo.8271327).

References

1. Abe, K. (1979). Size of great earthquakes of 1837–1974 inferred from tsunami data. Journal of Geophysical Research: Solid Earth, 84(B4), 1561-1568.

2. Aki, K., & Lee, W. H. K. (1976). Determination of three-dimensional velocity anomalies under a seismic array using first P arrival times from local earthquakes: 1. A homogeneous initial model. Journal of Geophysical research, 81(23), 4381-4399.

3. Aki, K., Christoffersson, A., & Husebye, E. S. (1977). Determination of the three-dimensional seismic structure of the lithosphere. Journal of Geophysical Research, 82(2), 277-296.

4. Altamimi, Z., Rebischung, P., Métivier, L., & Collilieux, X. (2016). ITRF2014: A new release of the International Terrestrial Reference Frame modeling nonlinear station motions. *Journal of geophysical research: solid earth*, *121*(8), 6109-6131.

5. Angermann, D., Klotz, J., & Reigber, C. (1999). Space-geodetic estimation of the Nazca-South America Euler vector. Earth and Planetary Science Letters, 171(3), 329-334.

6. Arabasz Jr, W. J. (1971). Geological and geophysical studies of the Atacama fault zone in northern Chile. Doctoral dissertation, California Institute of Technology.

7. Arabasz, W. J. (1968). Geologic structure of the Taltal Area, Northern Chile, in relation to the earthquake of December 28, 1966. *Bulletin of the Seismological Society of America*, *58*(3), 835-842.

8. Araya-Vargas, J., Meqbel, N. M., Ritter, O., Brasse, H., Weckmann, U., Yáñez, G., & Godoy, B. (2019). Fluid distribution in the Central Andes subduction zone imaged with magnetotellurics. Journal of Geophysical Research: Solid Earth, 124(4), 4017-4034.

9. Barrientos, S. (2018). The seismic network of Chile. Seismological Research Letters, 89(2A), 467-474.

10. Bascuñán, S., Arriagada, C., Le Roux, J., Deckart, K., 2016. Unraveling the Peruvian Phase of the Central Andes: Stratigraphy, sedimentology and geochronology of the Salar de Atacama Basin (22°30-23°S), northern Chile. Basin Res. 28, 365–392. https://doi.org/10.1111/bre.12114

11. Beck, S., Barrientos, S., Kausel, E., & Reyes, M. (1998). Source characteristics of historic earthquakes along the central Chile subduction Askew et Alzone. Journal of South American Earth Sciences, 11(2), 115-129.

12. Béjar-Pizarro, M., Carrizo, D., Socquet, A., Armijo, R., Barrientos, S., Bondoux, F., ... & Vigny, C. (2010). Asperities and barriers on the seismogenic zone in North Chile: state-of-the-art after the 2007 M w 7.7 Tocopilla earthquake inferred by GPS and InSAR data. Geophysical Journal International, 183(1), 390-406.

13. Bello-González, J. P., Contreras-Reyes, E., & Arriagada, C. (2018). Predicted path for hotspot tracks off South America since Paleocene times: Tectonic implications of ridge-trench collision along the Andean margin. *Gondwana Research*, *64*, 216-234.

14. Bloch, W., Kummerow, J., Salazar, P., Wigger, P., & Shapiro, S. A. (2014). High-resolution image of the North Chilean subduction zone: seismicity, reflectivity and fluids. *Geophysical Journal International*, *197*(3), 1744-1749.

15. Brocher, T. M. (2005). Empirical relations between elastic wavespeeds and density in the Earth's crust. Bulletin of the seismological Society of America, 95(6), 2081-2092.

16. Calle-Gardella, D., Comte, D., Farías, M., Roecker, S., & Rietbrock, A. (2021). Three-dimensional local earthquake tomography of pre-Cenozoic structures in the coastal margin of central Chile: Pichilemu fault system. Journal of Seismology, 25(2), 521-533.

17. Calvert, A., Sandvol, E., Seber, D., Barazangi, M., Roecker, S., Mourabit, T., ... & Jabour, N. (2000). Geodynamic evolution of the lithosphere and upper mantle beneath the Alboran region of the western Mediterranean: Constraints from travel time tomography. *Journal of Geophysical Research: Solid Earth*, *105*(B5), 10871-10898.

18. Camus, F., & Dilles, J. H. (2001). A special issue devoted to porphyry copper deposits of northern Chile. *Economic Geology*, *96*(2), 233-237.

19. Cembrano, J., González, G., Arancibia, G., Ahumada, I., Olivares, V., & Herrera, V. (2005). Fault zone development and strain partitioning in an extensional strike-slip duplex: A case study from the Mesozoic Atacama fault system, Northern Chile. Tectonophysics, 400(1-4), 105-125.

20. Chen, H., & Wu, C. (2020). Metallogenesis and major challenges of porphyry copper systems above subduction zones. *Science China Earth Sciences*, *63*, 899-918.

21. Chlieh, M., De Chabalier, J. B., Ruegg, J. C., Armijo, R., Dmowska, R., Campos, J., & Feigl, K. L. (2004). Crustal deformation and fault slip during the seismic cycle in the North Chile subduction zone, from GPS and InSAR observations. *Geophysical Journal International*, *158*(2), 695-711.

22. Christensen, N. I. (1996). Poisson's ratio and crustal seismology. Journal of Geophysical Research: Solid Earth, 101(B2), 3139-3156.

23. Collot, J. Y., Marcaillou, B., Sage, F., Michaud, F., Agudelo, W., Charvis, P., ... & Spence, G. (2004). Are rupture zone limits of great subduction earthquakes controlled by upper plate structures? Evidence from multichannel seismic reflection data acquired across the northern Ecuador–southwest Colombia margin. *Journal of Geophysical Research: Solid Earth*, *109*(B11).

24. Comte, D., & Pardo, M. (1991). Reappraisal of great historical earthquakes in the northern Chile and southern Peru seismic gaps. Natural hazards, 4(1), 23-44.

25. Comte, D., Carrizo, D., Roecker, S., Ortega-Culaciati, F., & Peyrat, S. (2016). Three-dimensional elastic wave speeds in the northern Chile subduction zone: variations in hydration in the supraslab mantle. Geophysical Supplements to the Monthly Notices of the Royal Astronomical Society, 207(2), 1080-1105.

26. Comte, D., Farías, M., Calle-Gardella, D., Navarro-Aranguiz, A., Roecker, S., & Rietbrock, A. (2023). Anomalous intraslab structure revealed by the analysis of aftershocks of the Mw 6.7 Coquimbo-La Serena earthquake of 20 January 2019. *Tectonophysics*, *846*, 229660.

27. Comte, D., Farias, M., Roecker, S., & Russo, R. (2019). The nature of the subduction wedge in an erosive margin: Insights from the analysis of aftershocks of the 2015 Mw 8.3 Illapel earthquake beneath the Chilean Coastal Range. Earth and Planetary Science Letters, 520, 50-62.

28. Comte, D., Haessler, H., Dorbath, L., Pardo, M., Monfret, T., Lavenu, A., ... & Hello, Y. (2002). Seismicity and stress distribution in the Copiapo, northern Chile subduction zone using combined on-and off-shore seismic observations. Physics of the earth and planetary interiors, 132(1-3), 197-217.

29. Comte, D., Palma, G., Vargas, J. *et al.* Imaging the subsurface architecture in porphyry copper deposits using local earthquake tomography. *Sci Rep* **13**, 6812 (2023). https://doi.org/10.1038/s41598-023-33820-w

30. Contreras-Reyes, E., & Carrizo, D. (2011). Control of high oceanic features and subduction channel on earthquake ruptures along the Chile–Peru subduction zone. *Physics of the Earth and Planetary Interiors*, *186*(1-2), 49-58.

31. Contreras-Reyes, E., Díaz, D., Bello-González, J. P., Slezak, K., Potin, B., Comte, D., ... & Ruiz, S. (2021). Subduction zone fluids and arc magmas conducted by lithospheric deformed regions beneath the central Andes. *Scientific reports*, *11*(1), 23078.

32. Cooke, D. R., Hollings, P., & Walshe, J. L. (2005). Giant porphyry deposits: characteristics, distribution, and tectonic controls. Economic geology, 100(5), 801-818.

33. Crameri, F., Shephard, G. E., & Heron, P. J. (2020). The misuse of colour in science communication. Nature communications, 11(1), 1-10.

34. de Ballore, F. D. M. (1913, January). Historia sísmica de los andes meridionales al sur del paralelo XVI. In Anales de la Universidad de Chile (No. 71, pp. ág-129).

35. Delouis, B., Monfret, T., Dorbath, L., Pardo, M., Rivera, L., Comte, D., ... & Cisternas, A. (1997). The Mw= 8.0 Antofagasta (northern Chile) earthquake of 30 July 1995: A precursor to the end of the large 1877 gap. *Bulletin of the Seismological Society of America*, *87*(2), 427-445.

36. Delouis, B., Pardo, M., Legrand, D., & Monfret, T. (2009). The M w 7.7 Tocopilla earthquake of 14 November 2007 at the southern edge of the northern Chile seismic gap: Rupture in the deep part of the coupled plate interface. Bulletin of the Seismological Society of America, 99(1), 87-94.

37. Delph, J. R., Ward, K. M., Zandt, G., Ducea, M. N., & Beck, S. L. (2017). Imaging a magma plumbing system from MASH zone to magma reservoir. Earth and Planetary Science Letters, 457, 313-324.

38. DeMets, C., Gordon, R. G., Argus, D. F., & Stein, S. (1990). Current plate motions. Geophysical journal international, 101(2), 425-478.

39. DeMets, C., Gordon, R. G., Argus, D. F., & Stein, S. (1994). Effect of recent revisions to the geomagnetic reversal time scale on estimates of current plate motions. Geophysical research letters, 21(20), 2191-2194.

40. Deschamps, A., H. Lyon-Caen, and R. Madariaga (1980). Etude du tremblement de terre de Taltal (Chili 1966) à partir des ondes sismiques de longue période. Ann. Geophys, 36(2),

41. Díaz, D., Brasse, H., & Ticona, F. (2012). Conductivity distribution beneath Lascar volcano (Northern Chile) and the Puna, inferred from magnetotelluric data. Journal of Volcanology and Geothermal Research, 217, 21-29.

42. Eberhart-Phillips, D. (1986). Three-dimensional velocity structure in northern California Coast Ranges from inversion of local earthquake arrival times. *Bulletin of the Seismological Society of America*, *76*(4), 1025-1052.

43. Fuenzalida, A., Schurr, B., Lancieri, M., Sobiesiak, M., & Madariaga, R. (2013). High-resolution relocation and mechanism of aftershocks of the 2007 Tocopilla (Chile) earthquake. *Geophysical Journal International*, *194*(2), 1216-1228.

44. Fukao, Y. (1992). Seismic tomogram of the Earth's mantle: geodynamic implications. *Science*, *258*(5082), 625-630.

45. GeoForschungsZentrum, D. (2006). IPOC Seismic Network.

46. González-Vidal, D., Moreno, M., Sippl, C., Baez, J. C., Ortega-Culaciati, F., Lange, D., ... & Heit, B. (2023). Relation between oceanic plate structure, patterns of interplate locking and microseismicity in the 1922 Atacama seismic gap. *Geophysical Research Letters*, *50*(15), e2023GL103565.

47. Götze, H. J., & Krause, S. (2002). The Central Andean gravity high, a relic of an old subduction complex?. Journal of South American Earth Sciences, 14(8), 799-811.

48. Götze, H. J., Lahmeyer, B., Schmidt, S., Strunk, S., & Araneda, M. (1990). Central Andes gravity data base. Eos, Transactions American Geophysical Union, 71(16), 401-407.

49. Greenfield, T., White, R. S., & Roecker, S. (2016). The magmatic plumbing system of the Askja central volcano, Iceland, as imaged by seismic tomography. *Journal of Geophysical Research: Solid Earth*, *121*(10), 7211-7229.

50. Haberland, C., & Rietbrock, A. (2001). Attenuation tomography in the western central Andes: A detailed insight into the structure of a magmatic arc. Journal of Geophysical Research: Solid Earth, 106(B6), 11151-11167.

51. Hacker, B. R., Abers, G. A., & Peacock, S. M. (2003a). Subduction factory 1. Theoretical mineralogy, densities, seismic wave speeds, and H2O contents. Journal of Geophysical Research: Solid Earth, 108(B1).

52. Hacker, B. R., Peacock, S. M., Abers, G. A., & Holloway, S. D. (2003b). Subduction factory 2. Are intermediate-depth earthquakes in subducting slabs linked to metamorphic dehydration reactions?. Journal of Geophysical Research: Solid Earth, 108(B1).

53. Hayes, G. P., Moore, G. L., Portner, D. E., Hearne, M., Flamme, H., Furtney, M., & Smoczyk, G. M. (2018). Slab2, a comprehensive subduction zone geometry model. *Science*, *362*(6410), 58-61.

54. Herrera, C., Pastén-Araya, F., Cabrera, L., Potin, B., Rivera, E., Ruiz, S., ... & Contreras-Reyes, E. (2023). Rupture properties of the 2020 M w 6.8 Calama (northern Chile) intraslab earthquake. Comparison with similar intraslab events in the region. *Geophysical Journal International*, *232*(3), 2070-2079.

55. Hicks, S. P., Rietbrock, A., Ryder, I. M., Lee, C. S., & Miller, M. (2014). Anatomy of a megathrust: The 2010 M8. 8 Maule, Chile earthquake rupture zone imaged using seismic tomography. Earth and Planetary Science Letters, 405, 142-155.

56. Holtkamp, S. G., Pritchard, M. E., & Lohman, R. B. (2011). Earthquake swarms in South America. Geophysical Journal International, 187(1), 128-146.

57. Husen, S., Kissling, E., Flueh, E., & Asch, G. (1999). Accurate hypocentre determination in the seismogenic zone of the subducting Nazca Plate in northern Chile using a combined on-/offshore network. *Geophysical Journal International*, *138*(3), 687-701.

58. Husen, S., Kissling, E., & Flueh, E. R. (2000). Local earthquake tomography of shallow subduction in north Chile: A combined onshore and offshore study. Journal of Geophysical Research: Solid Earth, 105(B12), 28183-28198.

59. Husen, S., Kissling, E., & Quintero, R. (2002). Tomographic evidence for a subducted seamount beneath the Gulf of Nicoya, Costa Rica: The cause of the 1990 Mw= 7.0 Gulf of Nicoya earthquake. *Geophysical Research Letters*, *29*(8), 79-1.

60. Jarrin, P., Nocquet, J. M., Rolandone, F., Audin, L., Mora-Páez, H., Alvarado, A., ... & Cisneros, D. (2023). Continental block motion in the Northern Andes from GPS measurements. *Geophysical Journal International*, *235*(2), 1434-1464.

61. Inoue, H., Fukao, Y., Tanabe, K., & Ogata, Y. (1990). Whole mantle P-wave travel time tomography. *Physics of the Earth and Planetary Interiors*, *59*(4), 294-328.

62. Kanamori, H., Rivera, L., Ye, L., Lay, T., Murotani, S., & Tsumura, K. (2019). New constraints on the 1922 Atacama, Chile, earthquake from historical seismograms. Geophysical Journal International, 219(1), 645-661.

63. Kato, A., & Nakagawa, S. (2014). Multiple slow-slip events during a foreshock sequence of the 2014 Iquique, Chile Mw 8.1 earthquake. Geophysical Research Letters, 41(15), 5420-5427.

64. Kausel, E., & Campos, J. (1992). The Ms= 8 tensional earthquake of 9 December 1950 of northern Chile and its relation to the seismic potential of the region. Physics of the earth and planetary interiors, 72(3-4), 220-235.

65. Kelleher, J. A. (1972). Rupture zones of large South American earthquakes and some predictions. Journal of Geophysical Research, 77(11), 2087-2103.

66. Kennett, B. L. N., & Engdahl, E. R. (1991). Traveltimes for global earthquake location and phase identification. Geophysical Journal International, 105(2), 429-465.

67. Kisslinger, C., & Engdahl, E. R. (1973). The interpretation of the Wadati diagram with relaxed assumptions. *Bulletin of the Seismological Society of America*, *63*(5), 1723-1736.

68. Klein, E., Metois, M., Meneses, G., Vigny, C., & Delorme, A. (2018). Bridging the gap between North and Central Chile: insight from new GPS data on coupling complexities and the Andean sliver motion. *Geophysical Journal International*, *213*(3), 1924-1933.

69. Köther, N., Götze, H. J., Gutknecht, B. D., Jahr, T., Jentzsch, G., Lücke, O. H., ... & Zeumann, S. (2012). The seismically active Andean and Central American margins: Can satellite gravity map lithospheric structures?. Journal of Geodynamics, 59, 207-218.

70. Kühn, C., Brasse, H., & Schwarz, G. (2018). Three-dimensional electrical resistivity image of the volcanic arc in Northern Chile—an appraisal of early magnetotelluric data. Pure and Applied Geophysics, 175(6), 2153-2165.

71. Kushnir, A. F., Lapshin, V. M., Pinsky, V. I., & Fyen, J. (1990). Statistically optimal event detection using small array data. *Bulletin of the seismological society of america*, *80*(6B), 1934-1950.

72. Legrand, D., Delouis, B., Dorbath, L., David, C., Campos, J., Marquez, L., ... & Comte, D. (2007). Source parameters of the Mw= 6.3 Aroma crustal earthquake of July 24, 2001 (northern Chile), and its aftershock sequence. Journal of south American earth sciences, 24(1), 58-68.

73. León-Ríos, S., Bie, L., Agurto-Detzel, H., Rietbrock, A., Galve, A., Alvarado, A., ... & Woollam, J. (2021). 3D local earthquake tomography of the Ecuadorian margin in the source area of the 2016 Mw 7.8 Pedernales earthquake. Journal of Geophysical Research: Solid Earth, 126(3), e2020JB020701.

74. Leon-Rios, S. (2023). Research data for Taltal segment tomography article [Data set]. Zenodo. https://doi.org/10.5281/zenodo.8271327.

75. Lindsay, J. M., de Silva, S., Trumbull, R., Emmermann, R., & Wemmer, K. (2001). La Pacana caldera, N. Chile: a re-evaluation of the stratigraphy and volcanology of one of the world's largest resurgent calderas. *Journal of Volcanology and Geothermal Research*, *106*(1), 145–173. https://doi.org/https://doi.org/10.1016/S0377-0273(00)00270-5

76. Maksymowicz, A. (2015). The geometry of the Chilean continental wedge: Tectonic segmentation of subduction processes off Chile. Tectonophysics, 659, 183-196.

77. Marcaillou, B., Collot, J. Y., Ribodetti, A., d'Acremont, E., Mahamat, A. A., & Alvarado, A. (2016). Seamount subduction at the North-Ecuadorian convergent margin: Effects on structures, inter-seismic coupling and seismogenesis. *Earth and Planetary Science Letters*, *433*, 146-158.

78. Mavor, S. P., Singleton, J. S., Gomila, R., Heuser, G., Seymour, N. M., Williams, S. A., ... & Stockli, D. F. (2020). Timing, kinematics, and displacement of the Taltal fault system, northern Chile: Implications for the Cretaceous tectonic evolution of the Andean margin. Tectonics, 39(2), e2019TC005832.

79. Meng, L., Huang, H., Bürgmann, R., Ampuero, J. P., & Strader, A. (2015). Dual megathrust slip behaviors of the 2014 Iquique earthquake sequence. Earth and Planetary Science Letters, 411, 177-187.

80. Métois, M., Socquet, A., & Vigny, C. (2012). Interseismic coupling, segmentation and mechanical behavior of the central Chile subduction zone. *Journal of Geophysical Research: Solid Earth*, *117*(B3).

81. Metois, M., Socquet, A., Vigny, C., Carrizo, D., Peyrat, S., Delorme, A., ... & Ortega, I. (2013). Revisiting the North Chile seismic gap segmentation using GPS-derived interseismic coupling. *Geophysical Journal International*, *194*(3), 1283-1294.

82. Metois, M., Vigny, C., & Socquet, A. (2016). Interseismic coupling, megathrust earthquakes and seismic swarms along the Chilean subduction zone (38–18 S). Pure and Applied Geophysics, 173(5), 1431-1449.

83. Mitchell, M. A., White, R. S., Roecker, S., & Greenfield, T. (2013). Tomographic image of melt storage beneath Askja Volcano, Iceland using local microseismicity. *Geophysical Research Letters*, *40*(19), 5040-5046.

84. Monfret, T., Dorbath, L., Caminade, J. P., Pardo, M., Comte, D., & Ponce, L. (1995). The July 30, Antofagasta earthquake: an ‘‘Hypocritical’’seismic event. EOS, Trans. Am. geophys. Un, 76(46), 427.

85. Montessus de Ballore F (1912) Historia sísmica de los Andes meridionales al sur del paralelo XVI. Imprenta Cervantes, Santiago, pp 545–591. Delouis, B., Monfret, T., Dorbath, L., Pardo, M., Rivera, L., Comte, D., ... & Cisternas, A. (1997). The Mw= 8.0 Antofagasta (northern Chile) earthquake of 30 July 1995: A precursor to the end of the large 1877 gap. Bulletin of the Seismological Society of America, 87(2), 427-445.

86. Niemeyer, H., Götze, J., Sanhueza, M., & Portilla, C. (2018). The Ordovician magmatic arc in the northern Chile-Argentina Andes between 21° and 26° south latitude. *Journal of South American Earth Sciences*, *81*, 204–214. https://doi.org/https://doi.org/10.1016/j.jsames.2017.11.016

87. Norabuena, E. O., Dixon, T. H., Stein, S., & Harrison, C. G. (1999). Decelerating Nazca-South America and Nazca-Pacific plate motions. Geophysical Research Letters, 26(22), 3405-3408.

88. Palacios, C., Ramírez, L. E., Townley, B., Solari, M., & Guerra, N. (2007). The role of the Antofagasta–Calama Lineament in ore deposit deformation in the Andes of northern Chile. Mineralium Deposita, 42(3), 301-308.

89. Pastén-Araya, F., Potin, B., Ruiz, S., Zerbst, L., Aden-Antoniów, F., Azúa, K., ... & Fuenzalida, A. (2021). Seismicity in the upper plate of the Northern Chilean offshore forearc: Evidence of splay fault south of the Mejillones Peninsula. Tectonophysics, 800, 228706.

90. Peyrat, S., Madariaga, R., Buforn, E., Campos, J., Asch, G., & Vilotte, J. P. (2010). Kinematic rupture process of the 2007 Tocopilla earthquake and its main aftershocks

from teleseismic and strong-motion data. Geophysical Journal International, 182(3), 1411-1430.

91. Pisarenko, V. F., Kushnir, A. F., & Savin, I. V. (1987). Statistical adaptive algorithms for estimation of onset moments of seismic phases. *Physics of the earth and planetary interiors*, *47*, 4-10.

92. Prévot, R., Roecker, S. W., Isacks, B. L., & Chatelain, J. L. (1991). Mapping of low P wave velocity structures in the subducting plate of the central New Hebrides, southwest Pacific. Journal of Geophysical Research: Solid Earth, 96(B12), 19825-19842.

93. Pritchard, M. E., De Silva, S. L., Michelfelder, G., Zandt, G., McNutt, S. R., Gottsmann, J., ... & Ward, K. M. (2018). Synthesis: PLUTONS: Investigating the relationship between pluton growth and volcanism in the Central Andes. Geosphere, 14(3), 954-982.

94. Rawles, C., & Thurber, C. (2015). A non-parametric method for automatic determination of P-wave and S-wave arrival times: application to local micro earthquakes. *Geophysical Journal International*, *202*(2), 1164-1179.

95. Rawlinson, N., & Spakman, W. (2016). On the use of sensitivity tests in seismic tomography. *Geophysical Journal International, 205(2), 1221-1243.*

96. Reutter, K. J., Scheuber, E., & Chong, G. (1996). The Precordilleran fault system of Chuquicamata, northern Chile: Evidence for reversals along arc-parallel strike-slip faults. Tectonophysics, 259(1-3), 213-228.

97. Reutter, K. J., Scheuber, E., & Helmcke, D. (1991). Structural evidence of orogen-parallel strike slip displacements in the Precordillera of northern Chile. Geologische Rundschau, 80(1), 135-153.

98. Reyes-Wagner, V., Comte, D., Roecker, S. W., & Rietbrock, A. (2023). CORREL: Automated Onset Estimation for Controlled-Source Seismic Experiments. *Pure and Applied Geophysics*, 1-15.

99. Richards, J. (2016). Clues to hidden copper deposits. *Nature Geoscience, 9(3), 195-196.*

100. Rietbrock, Andreas (2024): Taltal Seismological Network. [Dataset]. Karlsruhe Institute of Technology. DOI: 10.35097/dIDjKJPeUpZFWjbQ

101. Rietbrock, Andreas; Comte, Diana & Leon-Rios, Sergio (2020): Taltal temporary deployment. [Dataset]. International Federation of Digital Seismograph Networks. Dataset/Seismic Network. https://doi.org/10.7914/mc8r-ft72.

102. Riller, U., Götze, H. J., Schmidt, S., Trumbull, R. B., Hongn, F., & Petrinovic, I. A. (2006). Upper-crustal structure of the Central Andes inferred from dip curvature analysis of isostatic residual gravity. In The Andes (pp. 327-336). Springer, Berlin, Heidelberg.

103. Roecker, S., Thurber, C., & McPhee, D. (2004). Joint inversion of gravity and arrival time data from Parkfield: New constraints on structure and hypocenter locations near the SAFOD drill site. Geophysical Research Letters, 31(12).

104. Roecker, S., Thurber, C., Roberts, K., & Powell, L. (2006). Refining the image of the San Andreas Fault near Parkfield, California using a finite difference travel time computation technique. Tectonophysics, 426(1-2), 189-205.

105. Ruegg, J. C., Campos, J., Armijo, R., Barrientos, S., Briole, P., Thiele, R., ... & Serrurier, L. (1996). The Mw= 8.1 Antofagasta (North Chile) earthquake of July 30, 1995: first results from teleseismic and geodetic data. Geophysical Research Letters, 23(9), 917-920.

106. Ruiz, S., & Madariaga, R. (2018). Historical and recent large megathrust earthquakes in Chile. Tectonophysics, 733, 37-56.

107. Ruiz, S., Metois, M., Fuenzalida, A., Ruiz, J., Leyton, F., Grandin, R., ... & Campos, J. (2014). Intense foreshocks and a slow slip event preceded the 2014 Iquique Mw 8.1 earthquake. Science, 345(6201), 1165-1169.

108. Salazar, D., Easton, G., Goff, J., Guendon, J. L., González-Alfaro, J., Andrade, P., ... & Campos, J. (2022). Did a 3800-year-old M w~ 9.5 earthquake trigger major social disruption in the Atacama Desert?. Science advances, 8(14), eabm2996.

109. Scheuber, E., & Gonzalez, G. (1999). Tectonics of the Jurassic-Early Cretaceous magmatic arc of the north Chilean Coastal Cordillera (22–26 S): A story of crustal deformation along a convergent plate boundary. Tectonics, 18(5), 895-910.

110. Scholz, C. H., & Small, C. (1997). The effect of seamount subduction on seismic coupling. *Geology*, *25*(6), 487-490.

111. Schurr, B., & Rietbrock, A. (2004). Deep seismic structure of the Atacama basin, northern Chile. Geophysical Research Letters, 31(12).

112. Schurr, B., Rietbrock, A., Asch, G., Kind, R., & Oncken, O. (2006). Evidence for lithospheric detachment in the central Andes from local earthquake tomography. *Tectonophysics*, *415*(1-4), 203-223.

113. Sella, G. F., Dixon, T. H., & Mao, A. (2002). REVEL: A model for recent plate velocities from space geodesy. Journal of Geophysical Research: Solid Earth, 107(B4), ETG-11.

114. Sippl, C., Schurr, B., Asch, G., & Kummerow, J. (2018). Seismicity structure of the northern Chile forearc from> 100,000 double-difference relocated hypocenters. *Journal of Geophysical Research: Solid Earth*, *123*(5), 4063-4087.

115. Sippl, C., Schurr, B., Münchmeyer, J., Barrientos, S., & Oncken, O. (2023). The Northern Chile forearc constrained by 15 years of permanent seismic monitoring. *Journal of South American Earth Sciences*, 104326.

116. Ślęzak, K., Díaz, D., Vargas, J. A., Cordell, D., Reyes-Cordova, F., & Segovia, M. J. (2021). Magnetotelluric image of the Chilean subduction zone in the Salar de Atacama region (23°-24° S): Insights into factors controlling the distribution of volcanic arc magmatism. *Physics of the Earth and Planetary Interiors*, *318*, 106765.

117. Spakman, W., & Nolet, G. (1988). Imaging algorithms, accuracy and resolution in delay time tomography. *Mathematical geophysics: A survey of recent developments in seismology and geodynamics*, 155-187.

118. Tassara, A., & Echaurren, A. (2012). Anatomy of the Andean subduction zone: three-dimensional density model upgraded and compared against global-scale models. *Geophysical Journal International, 189(1), 161-168.*

119. Thurber, C. H., Atre, S. R., & Eberhart-Phillips, D. (1995). Three-dimensional Vp and Vp/Vs structure at Loma Prieta, California, from local earthquake tomography. *Geophysical Research Letters*, *22*(22), 3079-3082.

120. Tomlinson, A. J., & Blanco, N. (1997a). Structural evolution and displacement history of the west fault systems, Precordillera, Chile, part 1, Post-mineral history, paper presented at VIII Congreso Geológico Chileno. *Soc. Geol. de Chile, Antofagasta, Chile*.

121. Tomlinson, A. J., & Blanco, N. (1997b). Structural evolution and displacement history of the west fault systems, Precordillera, Chile, part 2, Post-mineral history, paper presented at VIII Congreso Geológico Chileno. *Soc. Geol. de Chile, Antofagasta, Chile*.

122. Valenzuela-Malebrán, C., Cesca, S., López-Comino, J. A., Zeckra, M., Krüger, F., & Dahm, T. (2022). Source mechanisms and rupture processes of the Jujuy seismic nest, Chile-Argentina border. Journal of South American Earth Sciences, 117, 103887.

123. Victor, P., Oncken, O., & Glodny, J. (2004). Uplift of the western Altiplano plateau: Evidence from the Precordillera between 20 and 21 S (northern Chile). Tectonics, 23(4).

124. Victor, P., Sobiesiak, M., Glodny, J., Nielsen, S. N., & Oncken, O. (2011). Long-term persistence of subduction earthquake segment boundaries: Evidence from Mejillones Peninsula, northern Chile. Journal of Geophysical Research: Solid Earth, 116(B2).

125. Von Huene, R., Corvalán, J., Flueh, E. R., Hinz, K., Korstgard, J., Ranero, C. R., & Weinrebe, W. (1997). Tectonic control of the subducting Juan Fernández Ridge on the Andean margin near Valparaiso, Chile. Tectonics, 16(3), 474-488.

126.Wadati, K., & Oki, S. (1933). On the travel time of earthquake waves.(Part II). Journal of the Meteorological Society of Japan. Ser. II, 11(1), 14-28.Ward, K. M., Delph, J. R., Zandt, G., Beck, S. L., & Ducea, M. N. (2017). Magmatic evolution of a Cordilleran flare-up and its role in the creation of silicic crust. Scientific reports, 7(1), 1-8.

127.Ward, K. M., Delph, J. R., Zandt, G., Beck, S. L., & Ducea, M. N. (2017). Magmatic evolution of a Cordilleran flare-up and its role in the creation of silicic crust. *Scientific reports*, *7*(1), 9047.

128.Ward, K. M., Zandt, G., Beck, S. L., Christensen, D. H., & McFarlin, H. (2014). Seismic imaging of the magmatic underpinnings beneath the Altiplano-Puna volcanic complex from the joint inversion of surface wave dispersion and receiver functions. *Earth and Planetary Science Letters*, *404*, 43-53.

129.Wessel, P., W. H. F. Smith, R. Scharroo, J. Luis, and F. Wobbe, Generic Mapping Tools: Improved Version Released, EOS Trans. AGU, 94(45), p. 409–410, 2013. doi:10.1002/2013EO450001.

130.Willis, B. (1929). Earthquake conditions in Chile. Carnegie Institution of Washington, 382, 178p.

131.Yáñez-Cuadra, V., Ortega-Culaciati, F., Moreno, M., Tassara, A., Krumm-Nualart, N., Ruiz, J., ... & Benavente, R. (2022). Interplate coupling and seismic potential in the Atacama Seismic Gap (Chile): Dismissing a rigid Andean sliver. *Geophysical Research Letters*, *49*(11), e2022GL098257.

Figure captions:

Figure 1. **a)** Seismotectonic setting of the study area. Solid black lines represent the extent of historical megathrust earthquakes in the area (Monfret et al., 1995; Ruegg et al., 1996; Delouis et al., 1997; Delouis et al., 2009; Peyrat et al., 2010; Bejar-Pizarro et al., 2010; Ruiz and Madariaga, 2018) and white star show the epicenter of the intraplate 1950 Calama earthquake (Kausel and Campos, 1992). Solid blue and green lines mark the main trend of

the Atacama and Domeyko Fault Systems, respectively. Segmented black lines represent crustal faults: COT, Calama-Olacapato-Toro; AGF, Achibarca-Galan fault ; TTF, Taltal fault; MF, Mejillones fault. Red triangles show the active volcanoes and segmented lines offshore indicate the projection of the Mejillones Fracture Zone (MFZ) and Taltal ridge (TTR). Black squares highlight major settlements in the region, TOC: Tocopilla, CAL: Calama, SPA: San Pedro de Atacama, ANF: Antofagasta, TAL: Taltal. **b)** Distribution of the temporary seismic experiment with 84 short period 4.5 Hz geophones (white triangles) recording at 200 sps. The network collected data for 8 months, between March and October 2020. Yellow squares indicate major mining operations in the area. Black squares represent settlements in the region.

Figure 2. Seismicity distribution for the Taltal segment. **a)** Map view with earthquakes as small circles colored according to depth. Yellow squares indicate major mining operations in the area. Red triangles represent the active volcanic arc. The ellipses show the Norwest lineaments L1, L2, L3 described in text. Black squares show the main settlements. MFZ: Mejillones Fracture Zone, TTR: Taltal Ridge, APMB: Altiplano-Puna Magmatic Body, LMB: Lazufre Magmatic Body, SdA: Salar de Atacama.

Figure 3. W-E profiles with the seismic distribution in depth. Inverted triangles represent the station distribution in the area. The volcanic arc is represented by red triangles. AFS: Atacama Fault System, DFS: Domeyko Fault System.

Figure 4. This is a daily test to analyze seismic activity in the Atacama Fault System (AFS) and the Domeyko Fault System (DFS). The profile displays seismicity and blasting identified near the AFS and DFS. The inset plot illustrates the distribution of activity in relation to local time.

Figure 5. Cross sections of the 3D velocity model for Vp **(left)** and Vp/Vs **(right).** Results are shown along 8 W-E profiles as shown in Figure 2. Vp velocities and Vp/Vs ratios are color-coded and isocontours are plotted every 0.25 km/s and 0.05 for Vp and Vp/Vs, respectively. Well-resolved areas are highlighted based on the resolution tests. Width for projection of hypocenters and stations is 20 km. Relocated hypocenters are plotted as white circles, and stations are represented by inverted triangles. Proposed slab interface (see text for further details) is represented by segmented blue line while slab 2.0 (Hayes et al., 2018) is shown with segmented black line. Segmented red (Vp) and grey (Vp/Vs) represent the inferred continental Moho. Red triangles indicate the position of the volcanic arc. AFS: Atacama Fault System, DFS: Domeyko Fault System; A1-A8, anomalies described in text.

Figure 6. 3D velocity models, Vp **(left)** and Vp/Vs **(right)** shown in horizontal slices at 10, 30, 50 and 110 km depth. Well-resolved areas are highlighted based on the model resolution tests. Red triangles indicate the position of the volcanic arc. Major mining operations are represented by yellow squares in the 10 km depth slices. Velocity anomalies collocated to surface observations in the text are also shown in the 10 km depth slice. Location of cross section profiles of Figure 3 are shown as black solid lines. Corresponding slab depth contour (Hayes et al., 2018) is represented by a thick gray line. Geological structures are plotted for the 10-30 km depths slices. MFZ: Mejillones Fracture Zone, TTR: Taltal Ridge, APMB: Altiplano-Puna Magmatic Body, LMB: Lazufre Magmatic Body, COT: Calama-Olacapato-Toro lineament, AGF: Achibarca-Galan fault, and TTF: Taltal fault. The anomalies labeled, A1-A8, are described in the text.

Figure 7. Zoom in to the Salar de Atacama (SdA). **a)** Overview of the region of interest. The red box indicates the area of zoom. **b)** North-south profile for the Vp/Vs model at latitude 68°W. Thick segmented line represents the slab interface. **c)** Map view the Vp/Vs model around the SdA. COT: Calama-Olacapato-Toro lineament.

Figure 8. Zoom in on to the volcanic related seismicity in P4-P5. **a)** The red box marks the area of interest. **b)** Vp/Vs profile showing the distribution of seismicity which coincides with an elevated (>1.80) Vp/Vs anomaly that suggests fluids moving upward to feed magmatic chambers of volcanos. Thick segmented line represents the slab interface. Red triangle shows the volcanic arc. A6: seismic anomaly described in text.

Figure 9. Zoom in on to clustered seismicity in P1. **a)** Vp/Vs profile as shown in Figure 5. The red box indicates the area of interest. **b)** Seismic activity distribution around the area of interest. C1 represents the clustered seismicity described in the main text. The red segmented lines indicate possible fracturing within the Nazca plate. **c)** Vp/Vs profile of the area of interest with the distribution of seismicity. The main text describes the seismic anomaly A3.

Figure 10. Summary cartoon sketching the major observations in the oceanic slab (a, b, and c) and in the upper plate (d) along the Taltal segment. **a)** Northern segment, transition from hydrated (solid red) to dehydrated (solid blue) Nazca plate. Red dot highlights a dip change inferred by observing the seismicity distribution. Segmented sub-vertical lines represent areas where cluster of seismicity occurs ~100 km depth. **b)** Central segment, representation of the full path of fluids in the region. (1)Water enters the oceanic slab through offshore faults, (2) fluids are transported along the slab to greater depths, (3) pressure and temperature ~50 km depths promote the release of fluids to the continental mantle, generating serpentinization, (4) partial melt occurs, and fluids can circulate upwards to feed magmatic chambers in the region. **c)** Southern segment, heights oceanic features from the Taltal ridge add stress to the marine forearc causing clustered seismicity. At greater depths, the dehydration of the plate contributes to having a serpentinized mantle and a highly hydrated upper plate. d) Upper plate with low Vp/Vs anomalies associated with the coastal cordillera and the metallogenic belt which are

separated by large-scale faults such as the Atacama and Domeyko fault system (AFS and DFS, respectively). Eastward, a high Vp/Vs anomaly is interpreted as fluids feeding the active volcanic arc in the region.

Figure 1.

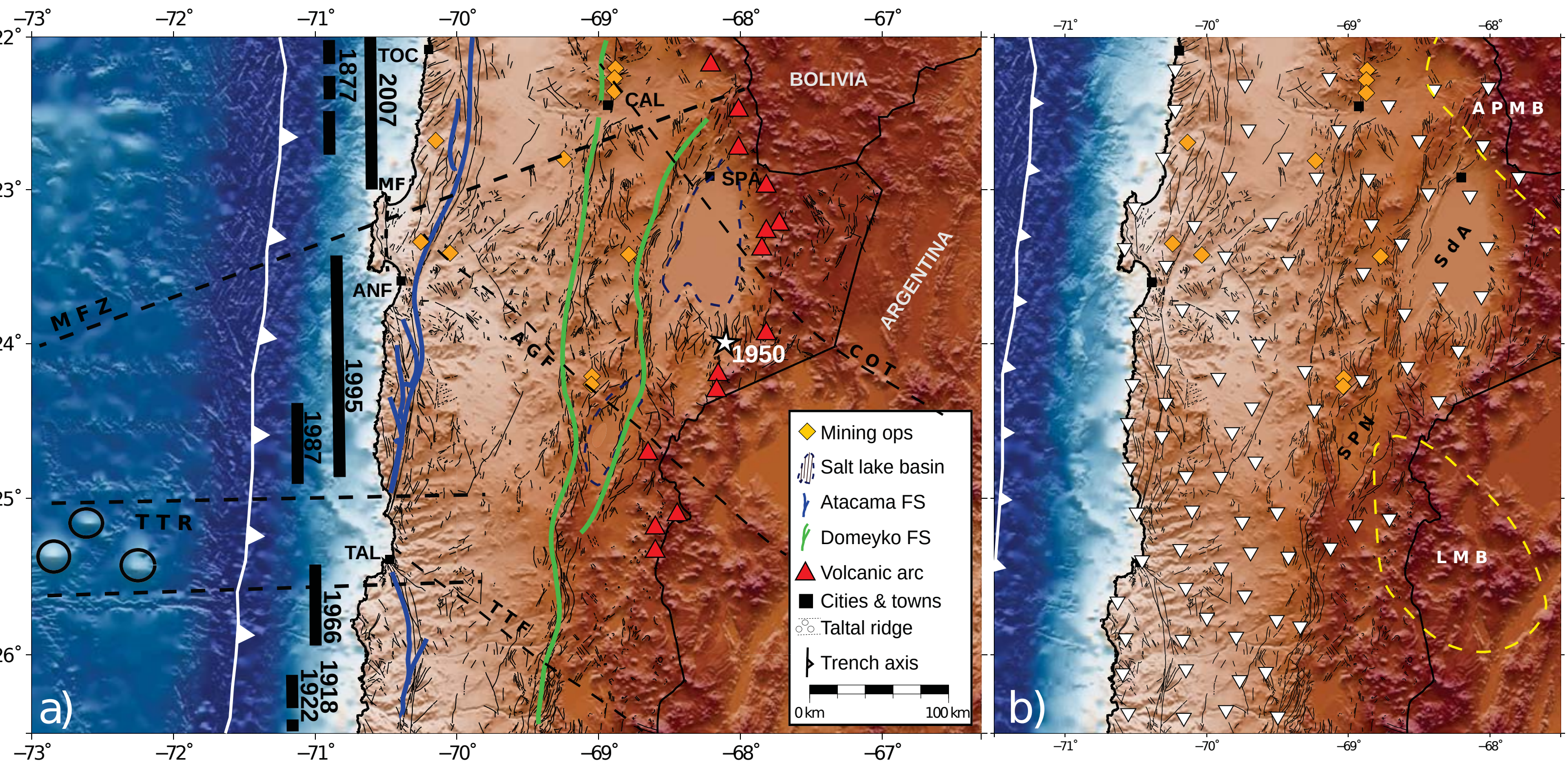

a)
b)
TOC
2007
1877
MF
CAL
SPA
BOLIVIA
ARGENTINA
ANF
MFZ
AGF
COT
1950
1995
1987
TTR
TAL
1966
1918
1922
TTF
Mining ops
Salt lake basin
Atacama FS
Domeyko FS
Volcanic arc
Cities & towns
Taltal ridge
Trench axis
0 km
100 km
APMB
SdA
SPN
LMB

Figure 2.

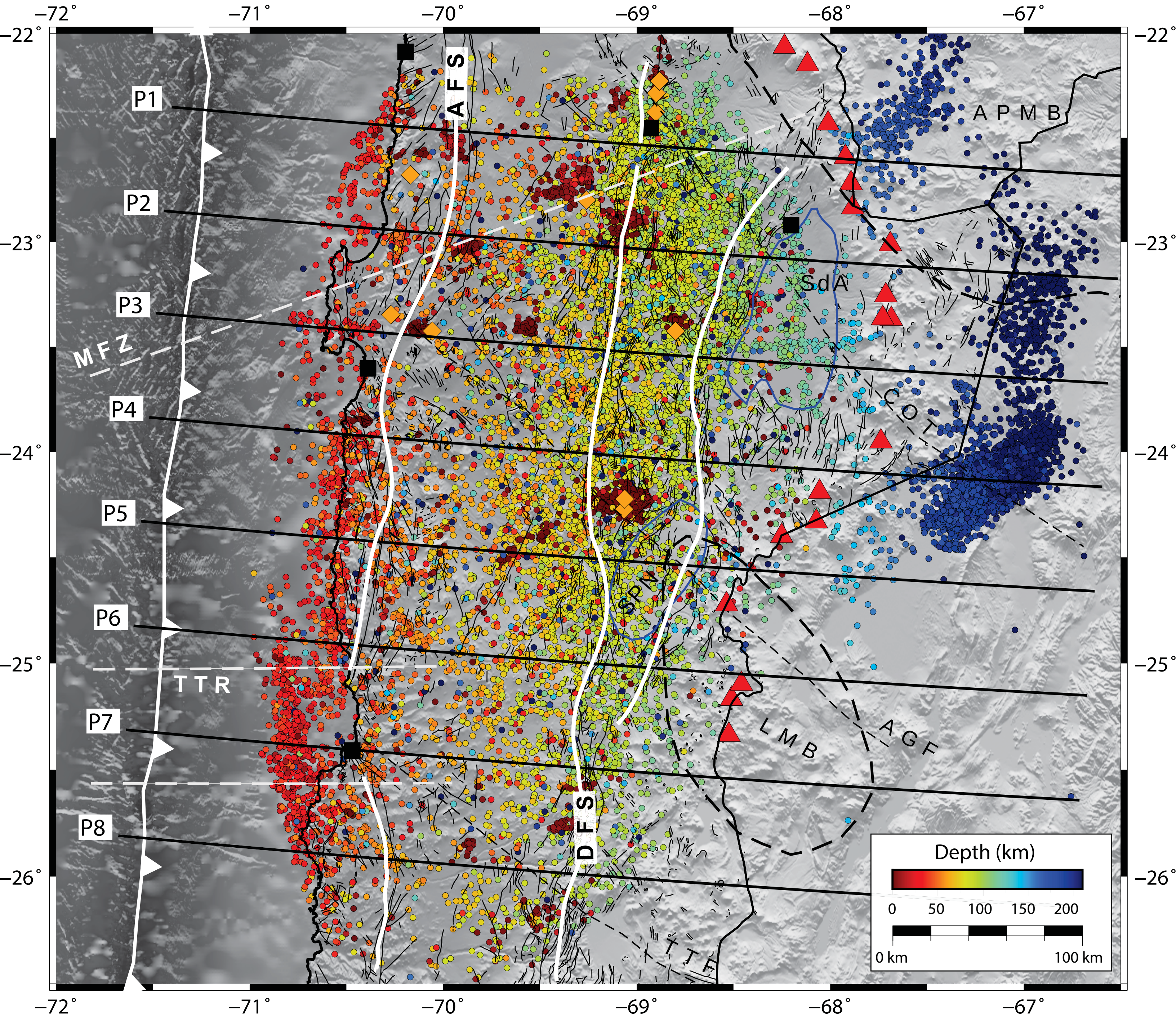

−72°
−71°
−70°
−69°
−68°
−67°
−22°
−23°
−24°
−25°
−26°
P1
P2
P3
P4
P5
P6
P7
P8
A F S
D F S
M F Z
T T R
A P M B
S d A
C O T
S P N
L M B
A G F
T T F
Depth (km)
0
50
100
150
200
0 km
100 km

Figure 3.

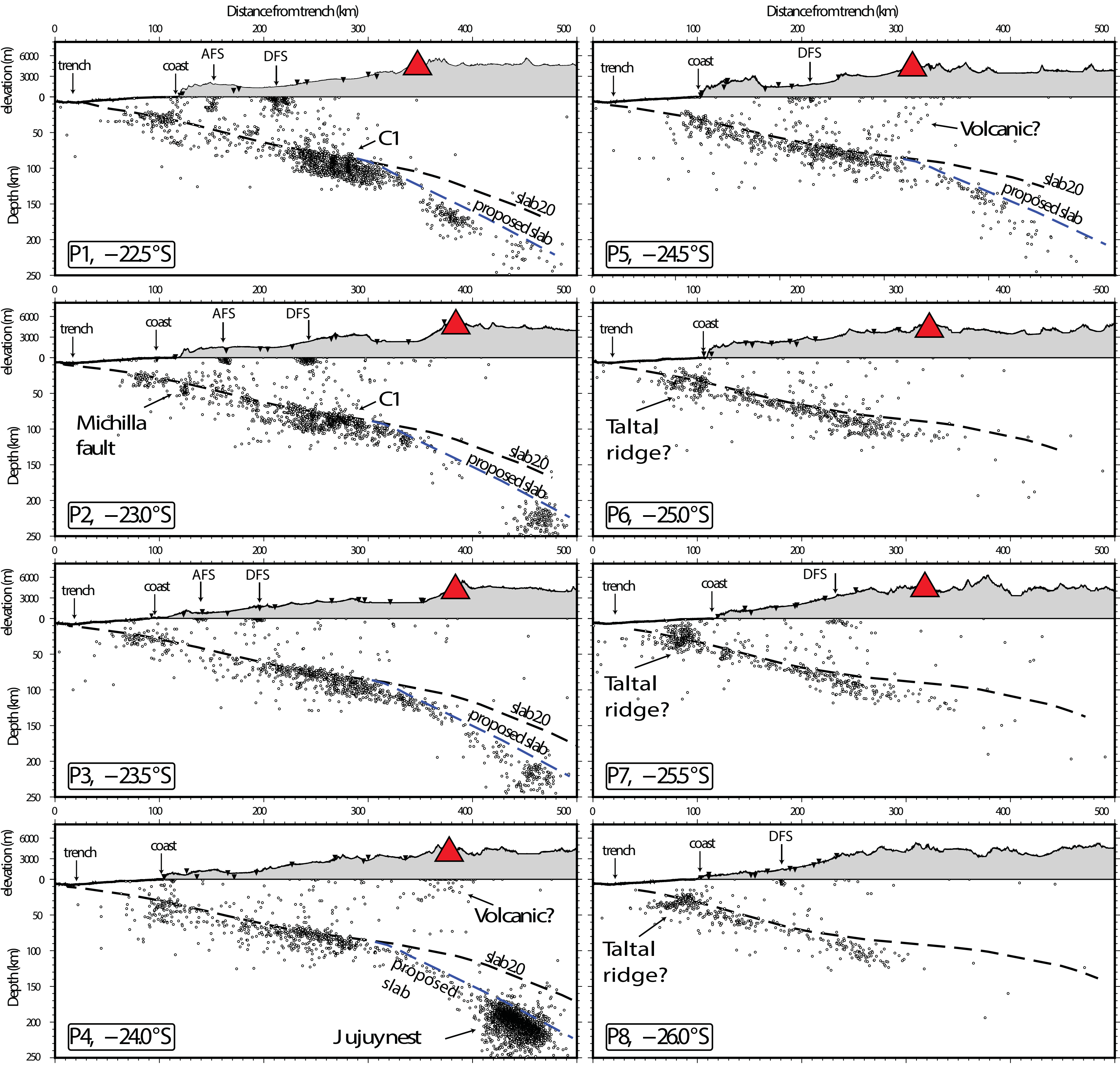
Distancefromtrench (km)
elevation (m)
Depth (km)
trench
coast
AFS
DFS
C1
slab20
proposed slab
P1, −22.5°S
Volcanic?
P5, −24.5°S
Michilla fault
P2, −23.0°S
Taltal ridge?
P6, −25.0°S
P3, −23.5°S
P7, −25.5°S
Jujuynest
P4, −24.0°S
P8, −26.0°S

Figure 4.

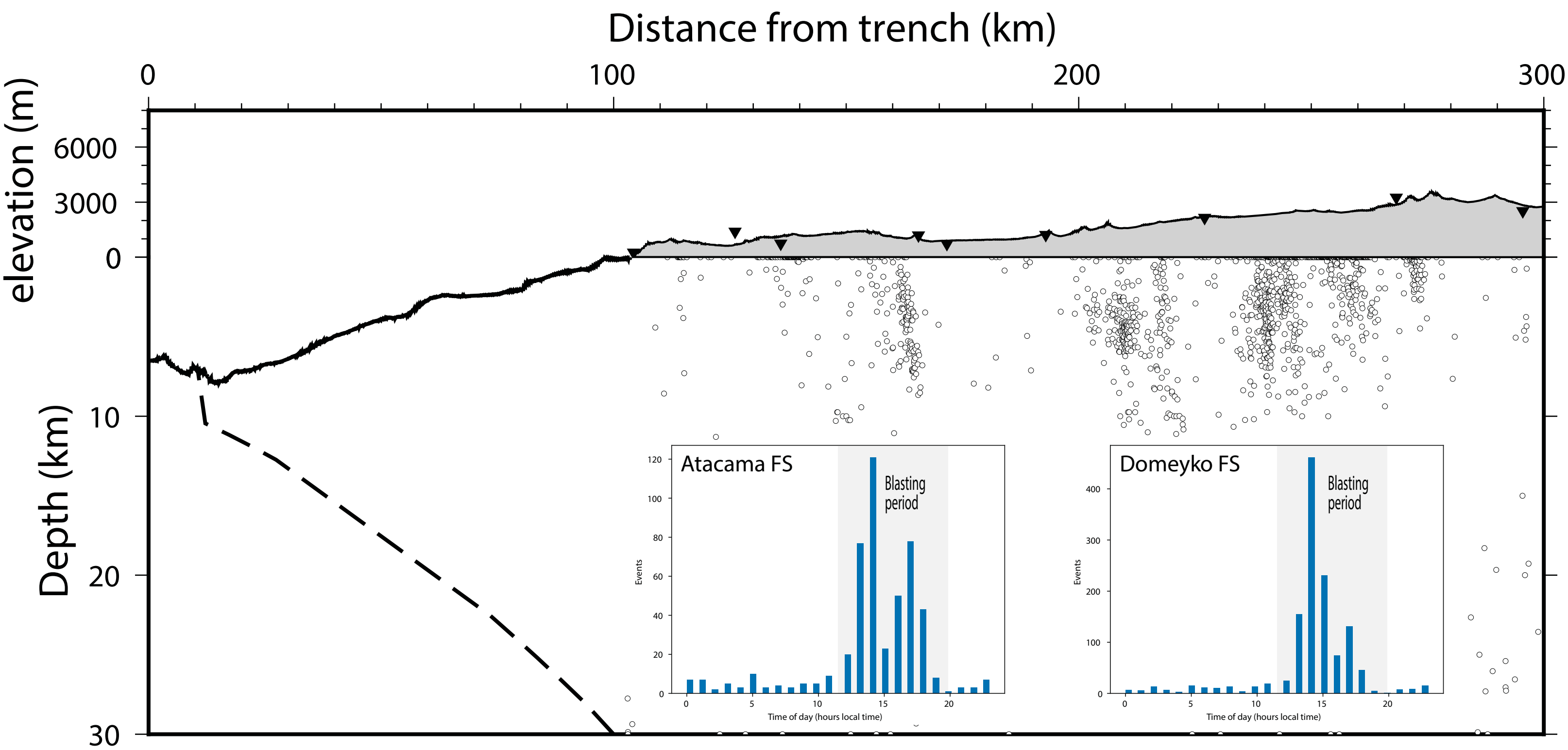

Distance from trench (km)
0
100
200
300
elevation (m)
6000
3000
0
Depth (km)
10
20
30
Atacama FS
Blasting period
Events
Time of day (hours local time)
Domeyko FS
Blasting period
Events
Time of day (hours local time)

Figure 5.

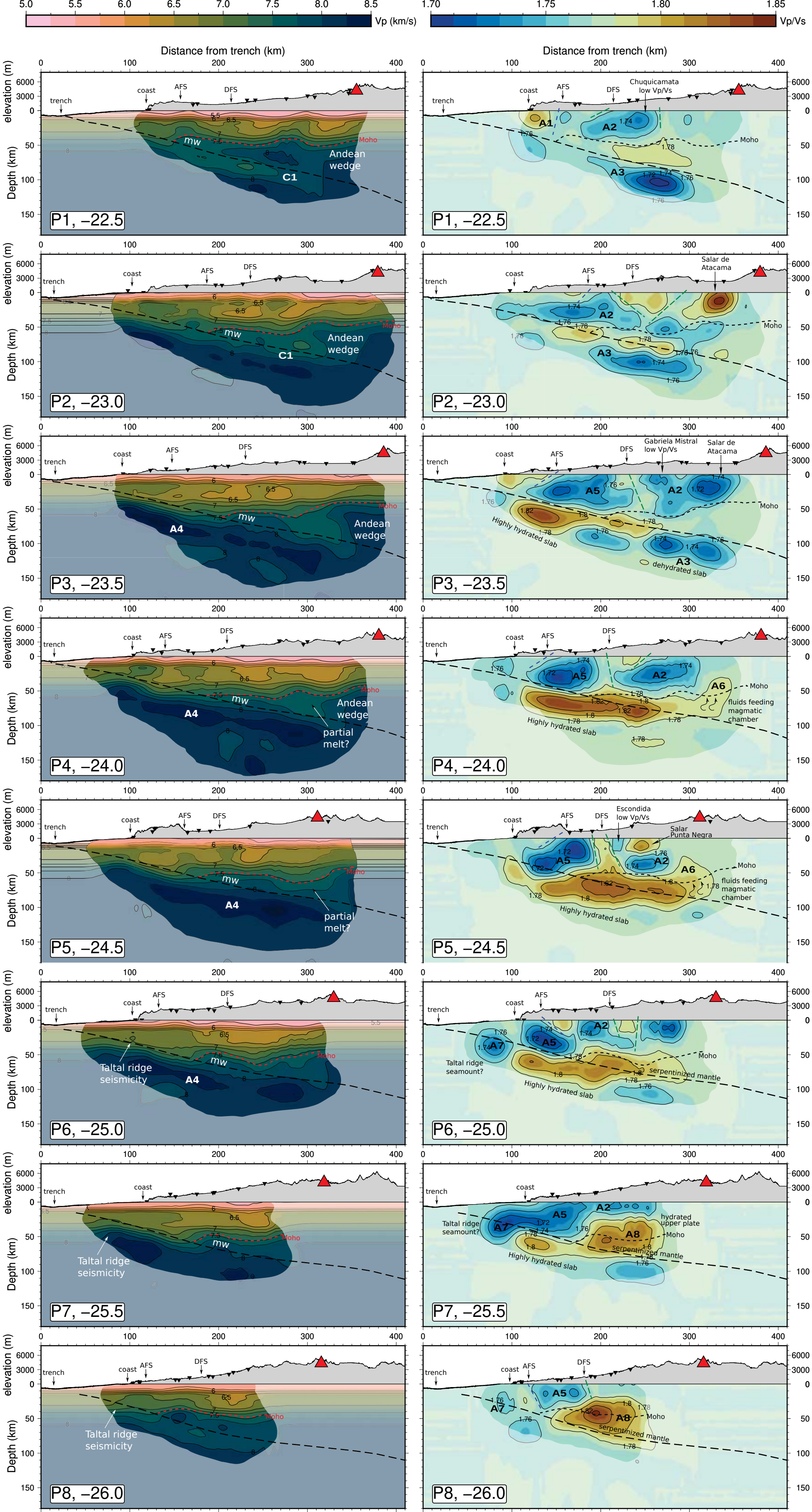

5.0 5.5 6.0 6.5 7.0 7.5 8.0 8.5
Vp (km/s)
1.70 1.75 1.80 1.85
Vp/Vs
Distance from trench (km)
elevation (m)
Depth (km)
trench
coast
AFS
DFS
Moho
mw
Andean wedge
C1
A4
partial melt?
Taltal ridge seismicity
Chuquicamata low Vp/Vs
Salar de Atacama
Gabriela Mistral low Vp/Vs
Escondida low Vp/Vs
Salar Punta Negra
A1
A2
A3
A5
A6
A7
A8
Highly hydrated slab
dehydrated slab
fluids feeding magmatic chamber
Taltal ridge seamount?
serpentinized mantle
hydrated upper plate
P1, −22.5
P2, −23.0
P3, −23.5
P4, −24.0
P5, −24.5
P6, −25.0
P7, −25.5
P8, −26.0

Figure 6.

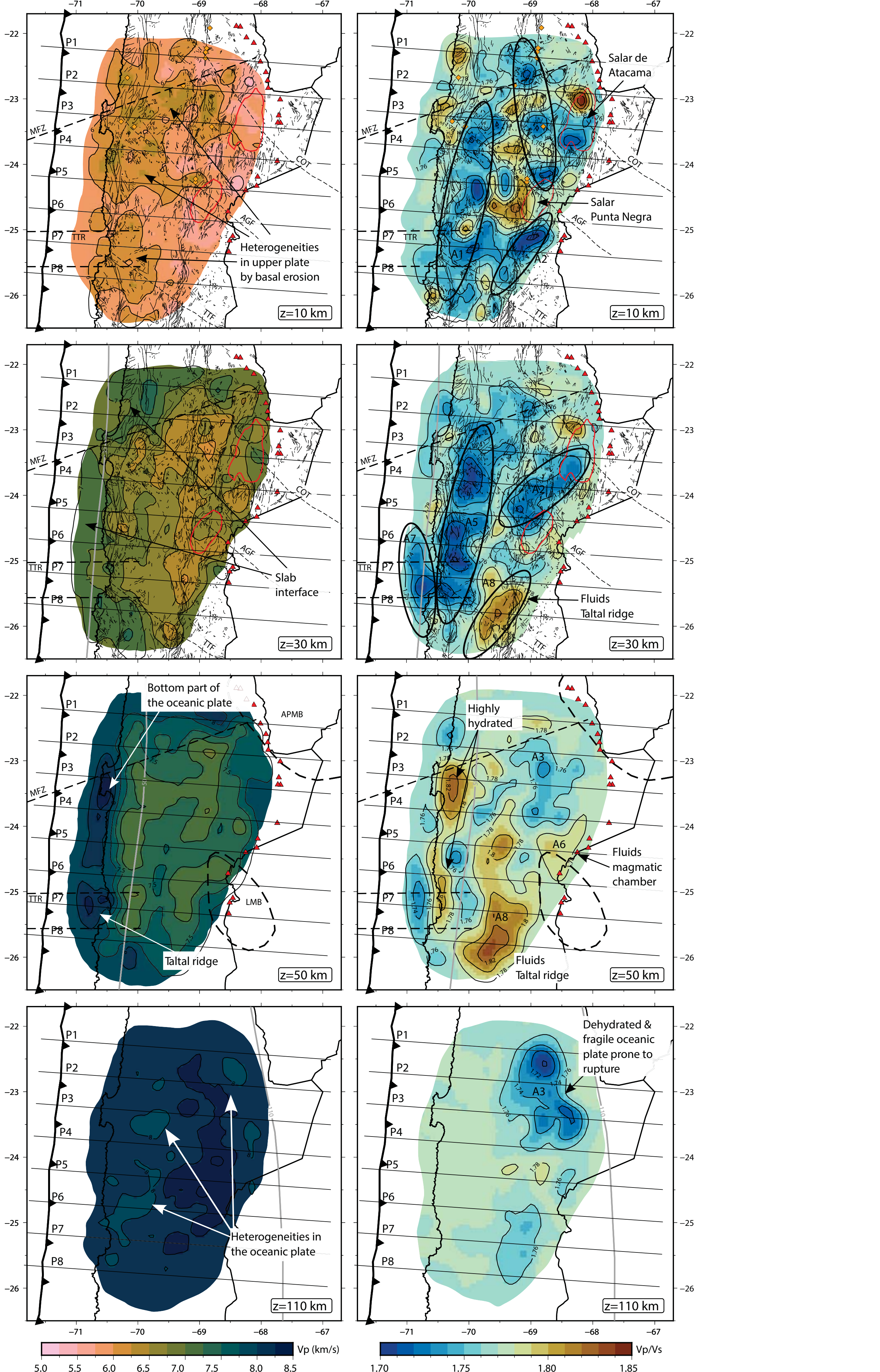

Salar de Atacama
Salar Punta Negra
Heterogeneities in upper plate by basal erosion
z=10 km
Slab interface
Fluids Taltal ridge
z=30 km
Bottom part of the oceanic plate
Taltal ridge
APMB
LMB
Highly hydrated
Fluids magmatic chamber
z=50 km
Dehydrated & fragile oceanic plate prone to rupture
Heterogeneities in the oceanic plate
z=110 km
MFZ
COT
AGF
TTR
TTF
Vp (km/s)
Vp/Vs

Figure 7.

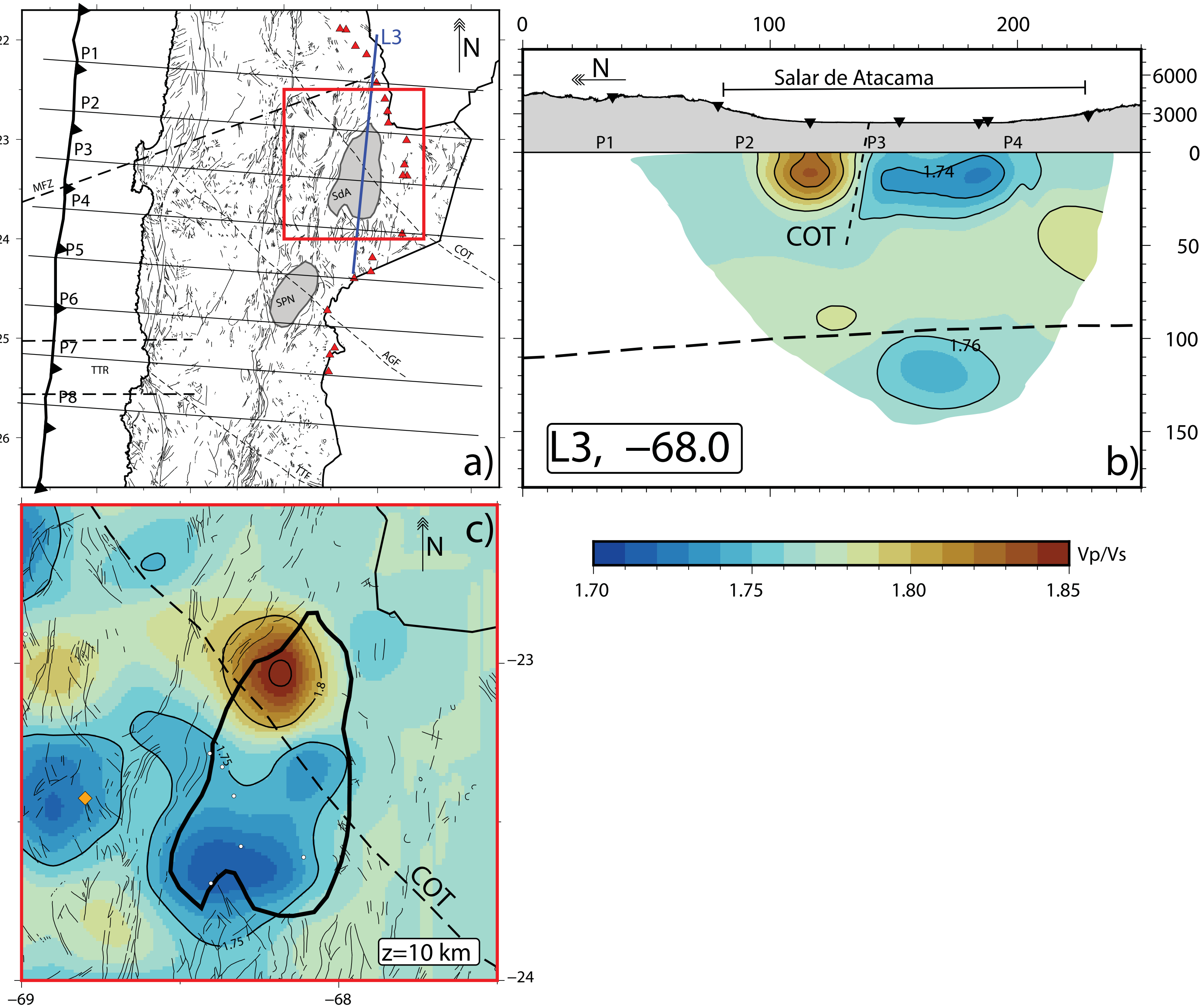

L3
N
P1
P2
P3
P4
P5
P6
P7
P8
MFZ
SdA
SPN
COT
AGF
TTR
TTF
a)
-22
-23
-24
-25
-26
0
100
200
Salar de Atacama
6000
3000
0
50
100
150
COT
1.74
1.76
L3, −68.0
b)
c)
1.8
1.75
COT
z=10 km
−69
−68
−23
−24
Vp/Vs
1.70
1.75
1.80
1.85

Figure 8.

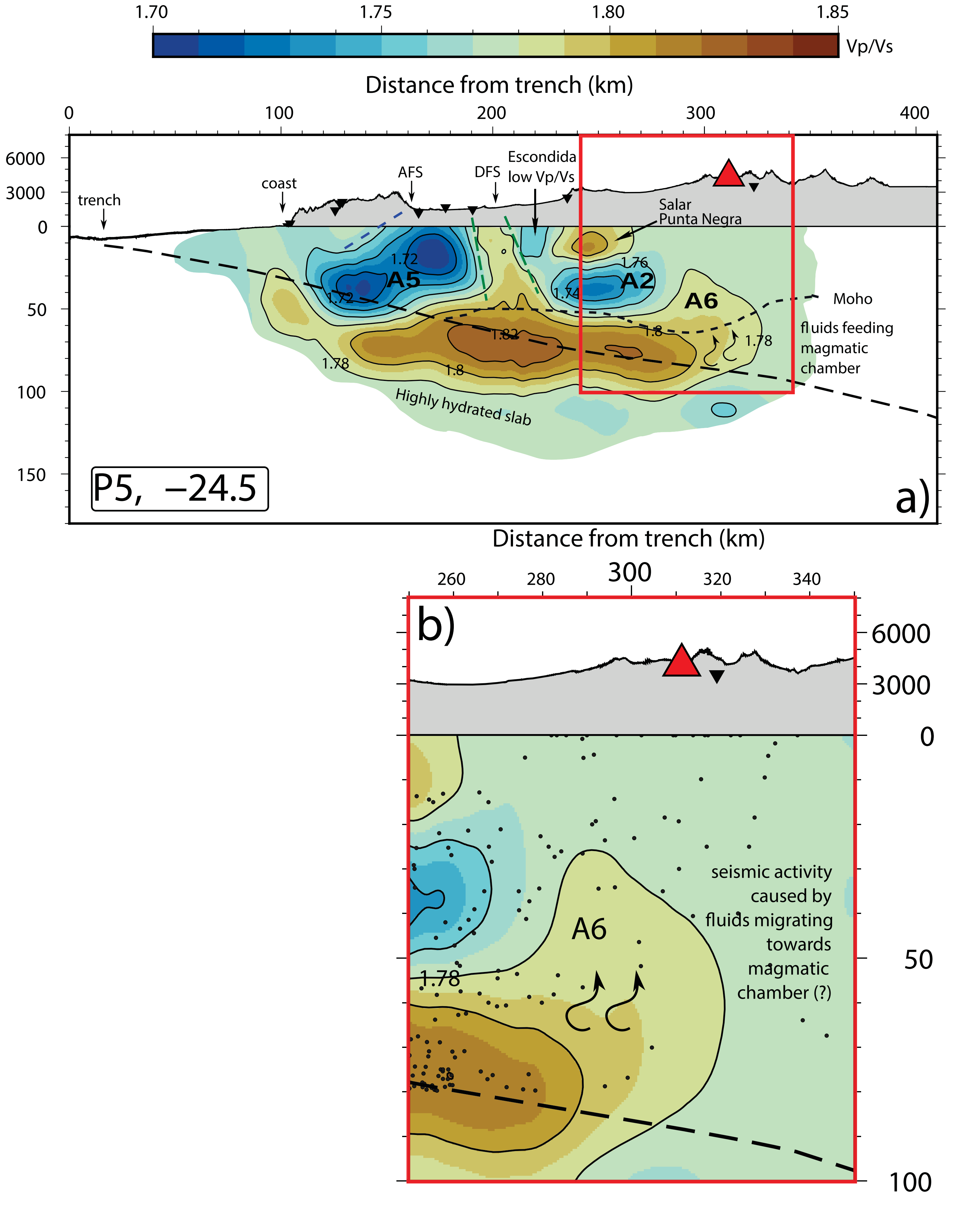
1.70
1.75
1.80
1.85
Vp/Vs
Distance from trench (km)
0
100
200
300
400
6000
3000
0
50
100
150
trench
coast
AFS
DFS
Escondida
low Vp/Vs
Salar
Punta Negra
1.72
A5
1.72
1.76
A2
1.74
A6
Moho
1.8
1.78
fluids feeding
magmatic
chamber
1.82
1.78
1.8
Highly hydrated slab
P5, –24.5
a)
Distance from trench (km)
260
280
300
320
340
b)
6000
3000
0
50
100
seismic activity
caused by
fluids migrating
towards
magmatic
chamber (?)
A6
1.78

Figure 9.

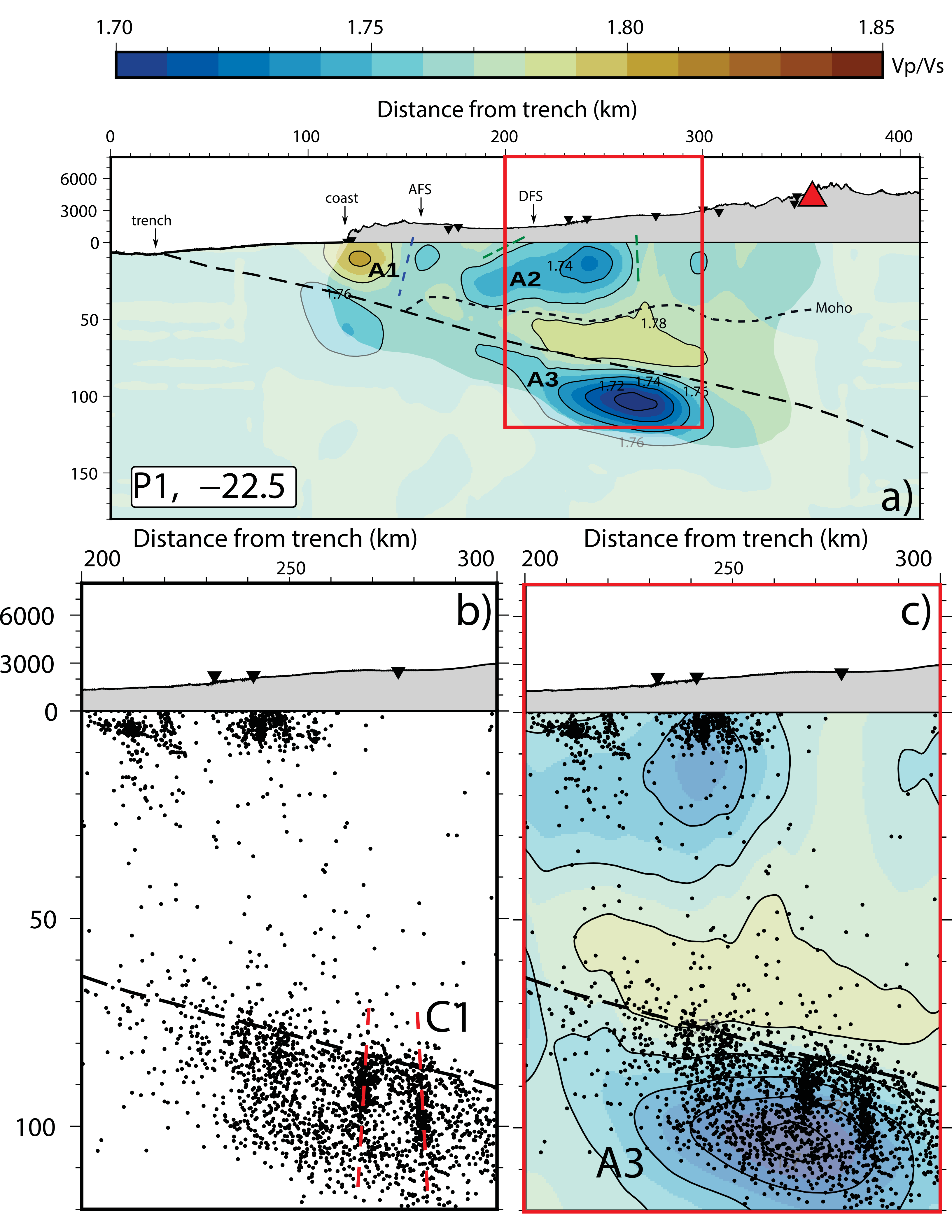

1.70
1.75
1.80
1.85
Vp/Vs
Distance from trench (km)
0
100
200
300
400
6000
3000
0
50
100
150
trench
coast
AFS
DFS
A1
A2
A3
1.74
1.76
1.78
1.72
1.75
Moho
P1, −22.5
a)
Distance from trench (km)
200
250
300
6000
3000
0
50
100
b)
C1
Distance from trench (km)
200
250
300
c)
A3

Figure 10.

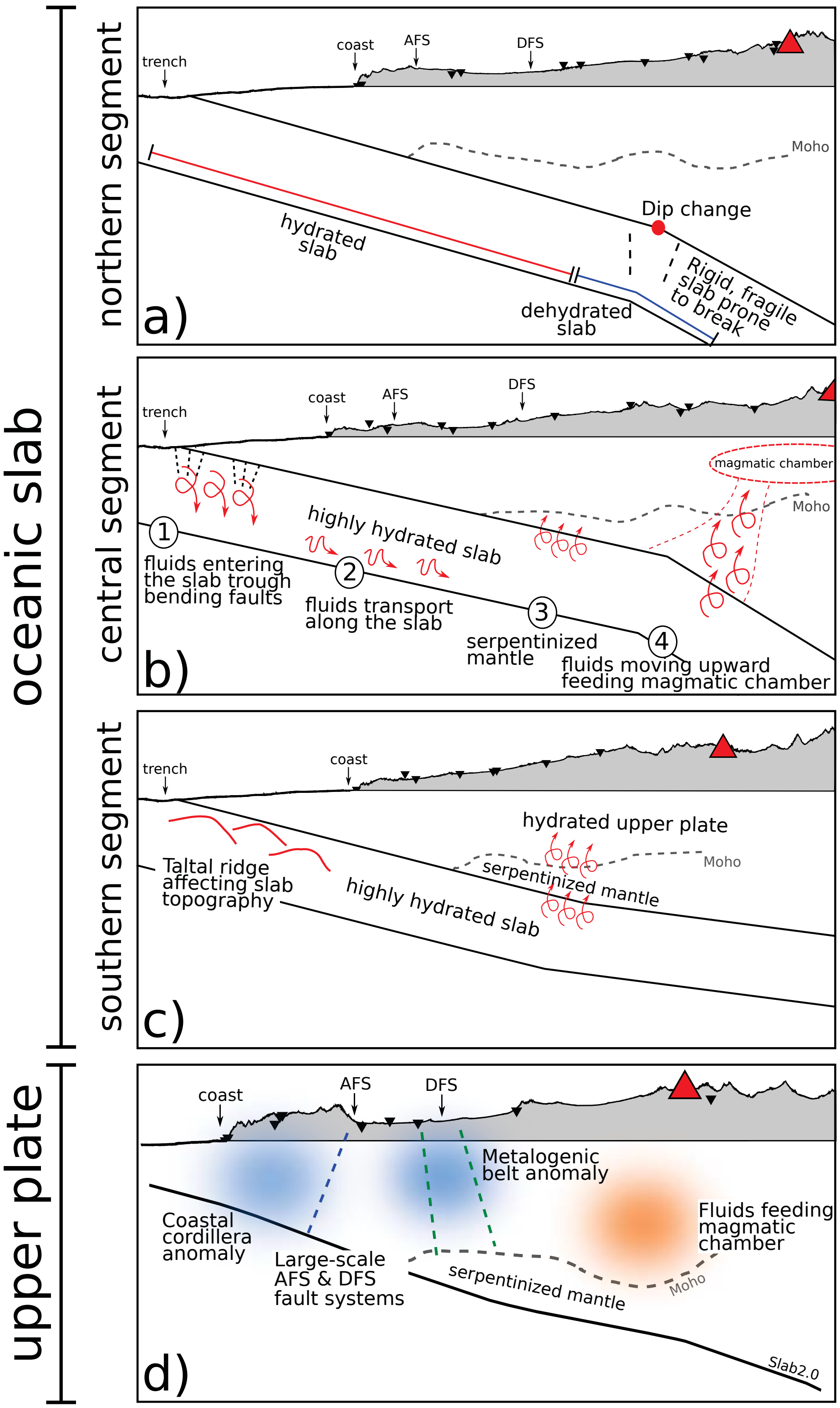
oceanic slab
upper plate
northern segment
central segment
southern segment
a)
trench
coast
AFS
DFS
Moho
Dip change
hydrated slab
dehydrated slab
Rigid, fragile slab prone to break
b)
trench
coast
AFS
DFS
magmatic chamber
Moho
highly hydrated slab
1
2
3
4
fluids entering the slab trough bending faults
fluids transport along the slab
serpentinized mantle
fluids moving upward feeding magmatic chamber
c)
trench
coast
hydrated upper plate
Moho
serpentinized mantle
Taltal ridge affecting slab topography
highly hydrated slab
d)
coast
AFS
DFS
Metalogenic belt anomaly
Coastal cordillera anomaly
Large-scale AFS & DFS fault systems
Fluids feeding magmatic chamber
serpentinized mantle
Moho
Slab2.0